Aalborg Universitet

AALBORG UNIVERSITY
DENMARK

Papers

Volume 6: 2001-2003

Thoft-Christensen, Palle

Publication date:
2007

Document Version
Publisher's PDF, also known as Version of record

Link to publication from Aalborg University

Citation for published version (APA):
Thoft-Christensen, P. (2007). *Papers: Volume 6: 2001-2003*. Department of Civil Engineering, Aalborg University.

General rights
Copyright and moral rights for the publications made accessible in the public portal are retained by the authors and/or other copyright owners and it is a condition of accessing publications that users recognise and abide by the legal requirements associated with these rights.

- Users may download and print one copy of any publication from the public portal for the purpose of private study or research.
- You may not further distribute the material or use it for any profit-making activity or commercial gain
- You may freely distribute the URL identifying the publication in the public portal -

Take down policy
If you believe that this document breaches copyright please contact us at vbn@aub.aau.dk providing details, and we will remove access to the work immediately and investigate your claim.

Downloaded from vbn.aau.dk on: May 14, 2024

CHAPTER 110

ACTIVE FLAP CONTROL OF LONG SUSPENSION BRIDGES[1]

H.I. Hansen & P. Thoft-Christensen
University of Aalborg, Aalborg, Denmark.

ABSTRACT

This article is an extended summary of a Ph.D. Thesis; see Hansen [1]. In the thesis theoretical and experimental effects of flap control on a bridge section are compared. Dynamics of long suspension bridges is summarized with special attention on the flutter phenomenon. The aerodynamic derivatives for a flat plate with flaps are derived based on the Theodorsen theory. Estimation of the flutter wind velocity is shown when both the Theodorsen method and the Air Material Command method are used. Three control algorithms are described, namely Classical Linear Optimal closed-loop control, Instantaneous Optimal closed-loop control and control with constant phase angles between the motion of the bridge section and the flap motions. Wind tunnel experiments are described and the experimental data are analysed. Finally the results of the wind tunnel experiments are compared to the theory.

1. INTRODUCTION

During the last decades the span length of suspension bridges has grown rapidly. The Akashi Kaikyo Bridge with span length 1,991 m was opened for traffic in April 1998 and it is so far the longest suspension bridge of the world. Another long suspension bridge which was opened for traffic in June 1998 is the Great Belt Bridge with span length 1,624 m. Of future ultra-long span suspension bridges that may be constructed can be mentioned the Messina Crossing with the span length 3,300 m and the crossing of the Gibraltar Straits with the span length 3,550 m; see Brown [2].

To increase the span length the suspension bridge can be optimized with regard to materials, deck shape and cables as described by Brown [2], Gimsing [3], Astiz [4],

[1] Journal of Structural Control, Vol. 8, No. 1, June 2001, pp. 33-82.

Ostenfeld [5] and Ostenfeld & Larsen [6]. Another possibility may be to introduce the intelligent bridge, where active control systems are used to limit the vibrations. A step in this direction is to introduce passive control systems, e.g. viscoelastic damping elements, tuned mass dampers and eccentric masses, as described by Ostenfeld & Larsen [6].

The main problem in designing ultra-long span suspension bridges is flutter, which is an aeroelastic phenomenon; see Astiz [4]. Flutter occurs when the bridge is exposed to a wind speed above a critical value called the flutter wind velocity. The oscillations in flutter are perpendicular to the wind direction and may be torsional, vertical or a combined torsional and vertical motion. The flutter wind velocity is decreased with decreasing structural stiffness and damping. The problem of flutter, therefore, becomes more important with increasing span lengths of bridges as flutter is closely related to the stiffness of the bridge, which in turn is dependent on the span length, see Madsen & Ostenfeld-Rosenthal [7].

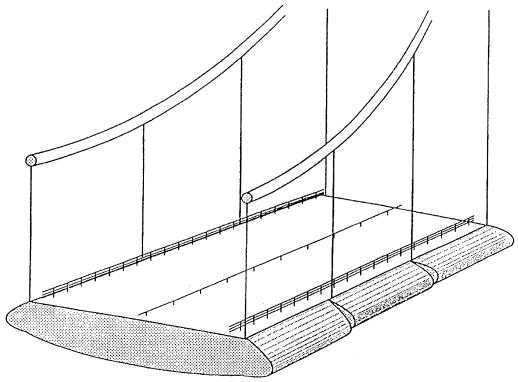

Figure 1.Flaps as integrated parts of the bridge girder.

COWI consult has patented a control system with actively controlled flaps in European Patent Specification [8]. The flaps are integrated in the bridge girder so each flap is the streamlined part of the edge of the girder, see figure 1. When the flaps are exposed to the wind they exert forces on the bridge girder. The directions and sizes of the forces can be regulated by regulating the flaps. By providing forces which counteract the motion of the girder the oscillations are damped.

A number of sensors are placed inside the bridge girder to measure the position or motion of the girder. The measurements are transmitted to the control unit, e.g. a computer. The flaps are regulated based on a control algorithm that uses the measurements. In this way the flaps can be regulated continuously to counteract the motion of the girder. The flaps are divided into sections in the longitudinal direction of the bridge, and each of these sections can be regulated independently. The overall safety of the active control system is increased by the number of main control units and thus the number of independent sections. It is not necessary to mount flaps to the bridge girder over the entire span of the bridge. They may be mounted where they have the greatest effect, i.e. where the girder has the largest deflections. For symmetric modes of oscillations the optimal place is about the central part of the span and for asymmetric modes the optimal places are near the quarter points of the span.

If the safety of a long suspension bridge has to rely on a control system it is preferred that such a system is passive. Active control systems for limitations of vibrations of civil engineering structures have primary been used to fulfil serviceability state and comfort demands. In this case failure of the control system is not critical for the users of the structure or the structure itself. Therefore, the reliability of such systems is of less importance. Active control systems may in the future be common elements in wind sensitive bridges to enhance the comfort of the users, see Ostenfeld & Larsen [6].

The safety of a suspension bridge is governed by its response to infrequent and extreme loading, e.g. when it is exposed to the flutter wind velocity. As a result the active control system in an *intelligent bridge* may remain in stand-by mode for many years and perhaps decades without being activated. In this case it is very important that the control system is reliable at the very moment the dimensioning load is acting on the structure. The reliability of the control system can be improved by making several independent systems with separated power supplies and by performing regular tests, e.g. by frequent use of the active control system also to fulfil serviceability state and comfort demands.

2. DYNAMICS OF LONG SUSPENSION BRIDGES

The motion-induced wind loads on a streamlined bridge deck with integrated flaps are described in section 2.1 by a number of coefficients called aerodynamic derivatives. For new bridge designs these coefficients must be estimated by wind tunnel tests or by numerical flow simulations. For flexible bridges the cross-sectional shape of the bridge deck is the most dominating factor on the wind loads; see Scanlan [9]. Therefore, bridge section models are used to estimate the aero- dynamic derivatives. During preliminary design the aerodynamic derivatives may be approximated by the values for a flat plate which are summarized in section 2.1.

Estimation of the flutter wind velocity by Theodorsen's method is described in section 2.2. The Air Material Command (AMC) method for estimating the necessary structural damping of the bridge section as a function of the mean wind velocity is described in section 2.3. As an example, the flutter wind velocity and necessary structural damping are estimated for the model used in the wind tunnel experiments. In the example the aerodynamic derivatives for a flat plate are used.

2.1 Wind loads on bridge section with flaps

A rather streamlined bridge section is investigated, see figure 2. As shown by Ostenfeld & Larsen [6], streamlining the bridge deck increases the flutter wind velocity. A coordinate system is defined in the centre of mass gravity CG of the bridge section. The x-axis is horizontal and defined to be positive in the direction of the trailing edge. The y-axis is horizontal and perpendicular to the x-axis. The z-axis is vertical and is defined to be positive downwards.

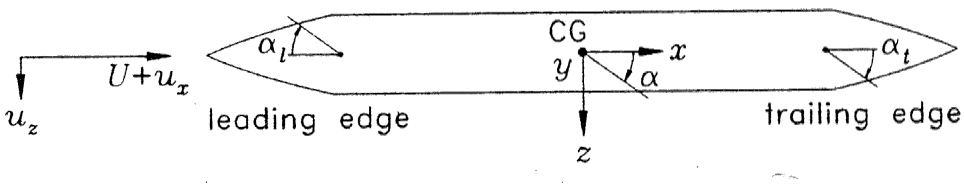

Figure 2. Definition of positive directions for bridge.

The bridge section is considered to be stiff and the motion in the direction of the *x*-axis is ignored. Thereby, the bridge section has two degrees of freedom, selected as the vertical displacement in the z-direction and the rotation α of the centre of mass gravity of the bridge section (positive clockwise). The angle α_t of the trailing flap and the

angle α_l of the leading flap are positive clockwise and refer to the undeflected position, i.e. relative to the bridge deck.

The modes that give coupled oscillations in vertical bending and torsion have their largest deflections in the same part of the bridge, i.e. the first symmetrical vertical bending mode may couple with the first symmetrical torsional mode; see Dyrbye & Hansen [10]. In the following it is assumed that the horizontal motion for the bridge deck is uncoupled with the bending/torsional motion. As described by Dyrbye & Hansen [10], the horizontal deflections may be significant for suspension bridges with very long spans. When the whole bridge span is analysed the following approach must therefore be extended by additional motion-induced load terms.

The wind is composed of a mean wind velocity *U*, measured in the undisturbed stream, and the turbulence components u_x and u_z, see figure 2. The turbulence component in the *y*-direction u_y is ignored. The stream around the model results in pressure differences on the upper and lower surface of the model. These pressure differences can be integrated into a load F^P (in the centre of mass gravity, positive downwards) and a moment F^M (positive clockwise) both per unit length in the *y*-direction.

The total wind load F_{tot} on a bridge section is composed of three components: the mean wind load F_U, wind load from turbulence F_u and the motion-induced (or aeroelastic) wind load F_a; see Dyrbye & Hansen [10].

$$F_{tot} = F_U + F_u + F_a \tag{1}$$

The suspension bridge must be designed to withstand the drag forces from the mean wind *U* and aeroelastic effects, such as torsional divergence, vortex-induced oscillation, flutter, galloping, and buffeting (caused by wind turbulence components *u)*; see Simiu & Scanlan [11]. For ultra-long span suspension bridges the main aeroelastic effect of concern is flutter; see Astiz [4] and Larsen & Walther [12]. In flutter the motion-induced wind load F_a is dominating in equation (1). Flutter occurs at a critical wind velocity at which the energy input from the motion-induced wind load is equal to the energy dissipated by structural damping; see Dyrbye & Hansen [10]. The critical wind velocity is called the flutter wind velocity U_f. The flutter phenomenon was first investigated in aerospace engineering and the relevant terms were carried over to wind engineering. Flutter of bridge sections is described by Simiu & Scanlan [11] and Larsen & Walther [12]:

- Single-degree flutter in torsion, also called stall flutter, is a pure torsional motion of the bridge section. The amplitude of the torsional oscillation grows with increasing wind velocity.
- Binary flutter, also called classical flutter, is a coupled vertical and torsional motion of the bridge section. Once the wind velocity exceeds the flutter wind velocity the oscillations grow to catastrophic amplitudes.

As described by Simiu & Scanlan [11], flutter may involve nonlinear aerodynamics. However, the flutter problem has been successfully solved by linear analysis methods. The motion-induced force F_a is divided into the motion-induced vertical load F_a^P and the motion-induced moment F_a^M. The equations of motion of a bridge section exposed to the motion-induced forces are

$$m(\ddot{z} + 2\zeta_z\omega_z\dot{z} + \omega_z^2 z) = F_a^P = F_{ad}^P + F_{at}^P + F_{al}^P \tag{2}$$

$$I(\ddot{\alpha} + 2\zeta_\alpha\omega_\alpha\dot{\alpha} + \omega_\alpha^2\alpha) = F_a^M = F_{ad}^M + F_{at}^M + F_{al}^M \tag{3}$$

where m and *I* are the mass and the mass moment of inertia, respectively, both per unit length, *z* denotes the vertical bending motion, α denotes the torsional motion, ς is the damping ratio and *w* is the undamped circular eigenfrequency. The motion-induced wind loads F_a^P and F_a^M are described by three components:

- Loads F_{ad}^P and F_{ad}^M due to movement of the bridge deck, see section 2.1.1
- Loads F_{at}^P and F_{at}^M due to movement of the trailing flap, see section 2.1.2.
- Loads F_{al}^P and F_{al}^M due to movement of the leading flap, see section 2.1.3.

2.1.1 *Loads due to Movement of Bridge Deck*

Based on principles of potential flow theory, Theodorsen [13] has shown that for thin airfoils (without flaps) in incompressible flow the expressions for F_{ad}^P and F_{ad}^M are linear in *z* and α and their first and second derivatives. Assuming harmonic vibrations at the frequency w the motion-induced forces due to movement of the bridge deck can be written; see Scanlan [9],

$$F_{ad}^P = \frac{1}{2}\rho U^2 B\left[KH_1^\star(K)\frac{\dot{z}}{U} + KH_2^\star(K)\frac{B\dot{\alpha}}{U} + K^2H_3^\star(K)\alpha + K^2H_4^\star(K)\frac{z}{B}\right] \quad (4)$$

$$F_{ad}^M = \frac{1}{2}\rho U^2 B^2\left[KA_1^\star(K)\frac{\dot{z}}{U} + KA_2^\star(K)\frac{B\dot{\alpha}}{U} + K^2A_3^\star(K)\alpha + K^2A_4^\star(K)\frac{z}{B}\right] \quad (5)$$

where *p* is the mass density of air, *B* is the width of the bridge section, $K = B\omega/U$ is the reduced frequency and $H_1^*,\ldots,H_4^*$, $A_1^*,\ldots,A_4^*$ are non-dimensional aerodynamic derivatives. The aerodynamic derivatives must be estimated by wind tunnel experiments or by numerical flow simulations, see Larsen & Walther [12]. During preliminary design of bridges the aerodynamic derivatives may be approximated by the corresponding values for a flat plate as derived by Theodorsen [13]. For a flat plate the aerodynamic derivatives are as follows:

$$H_1^\star(K) = -\frac{\pi F(k)}{k} \quad (6)$$

$$H_2^\star(K) = -\frac{\pi}{4k}\left[1 + F(k) + \frac{2G(k)}{k}\right] \quad (7)$$

$$H_3^\star(K) = -\frac{\pi}{2k^2}\left[F(k) - \frac{kG(k)}{2}\right] \quad (8)$$

$$H_4^\star(K) = \frac{\pi}{2}\left[1 + \frac{2G(k)}{k}\right] \quad (9)$$

$$A_1^\star(K) = \frac{\pi F(k)}{4k} \quad (10)$$

$$A_2^\star(K) = -\frac{\pi}{16k}\left[1 - F(k) - \frac{2G(k)}{k}\right] \quad (11)$$

$$A_3^\star(K) = \frac{\pi}{8k^2}\left[\frac{k^2}{8} + F(k) - \frac{kG(k)}{2}\right] \quad (12)$$

$$A_4^\star(K) = -\frac{\pi}{4}\frac{G(k)}{k} \quad (13)$$

where *F(k)* and *G(k)* are the real and imaginary parts of the Theodorsen circulatory function. The reduced frequency *k* is based on the half width of the bridge section, i.e. *k = K/2*. The aerodynamic derivatives are shown in figure 3 and figure 4 for a flat plate as functions of the reduced velocity *Ur* defined by

$$U_r = \frac{U}{fB} = \frac{2\pi U}{\omega B} = \frac{2\pi}{K} \tag{14}$$

where *f* is the frequency.

As seen in figures 3 and 4 the numerical values of the non-dimensional coefficients H_i^* and A_i^* are generally increasing with increasing reduced velocity.

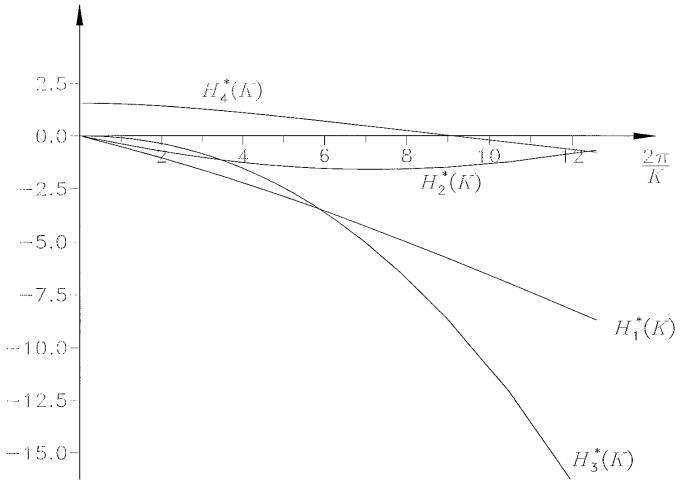

Figure 3. Aerodynamic derivatives for force on flat plate.

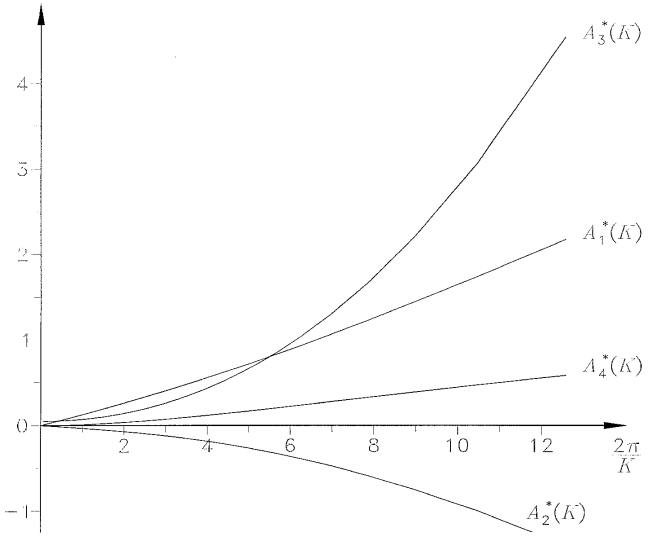

Figure 4. Aerodynamic derivatives for moment on flat plate.

2.1.2 *Loads due to Movement of Trailing Flap*

As for the bridge deck, Theodorsen [13] has shown that the loads due to movement of a trailing flap on a thin airfoil in incompressible flow are linear in the angle of the trailing flap at and the first and second derivatives. Assuming that the trailing flap is moved at

the same frequency w as the bridge deck, the motion induced forces due to movement of the trailing flap can be expressed by additional aerodynamic derivatives.

$$F_{at}^{P} = \frac{1}{2}\rho U^2 B\left[KH_5^{\star}(K)\frac{B\dot{\alpha}_t}{U} + K^2 H_6^{\star}(K)\alpha_t\right] \tag{15}$$

$$F_{at}^{M} = \frac{1}{2}\rho U^2 B^2\left[KA_5^{\star}(K)\frac{B\dot{\alpha}_t}{U} + K^2 A_6^{\star}(K)\alpha_t\right] \tag{16}$$

where $H_5^*(K)$, $H_6^*(K)$, $A_5^*(K)$ and $A_6^*(K)$ are aerodynamic derivatives. For a flat plate with a trailing flap the derivatives are

$$H_5^{\star}(K) = \frac{1}{4k}\left[T_4 - F(k)T_{11} - \frac{2G(k)T_{10}}{k}\right] \tag{17}$$

$$H_6^{\star}(K) = \frac{1}{4k^2}\left[-k^2 T_1 - 2F(k)T_{10} + kG(k)T_{11}\right] \tag{18}$$

$$A_5^{\star}(K) = \frac{1}{8k}\left[-\left(T_1 - T_8 - cT_4 + \frac{T_{11}}{2}\right) + \frac{F(k)T_{11}}{2} + \frac{G(k)T_{10}}{k}\right] \tag{19}$$

$$A_6^{\star}(K) = \frac{1}{8k^2}\left[-(T_4 + T_{10}) - k^2(T_7 + cT_1) + F(k)T_{10} - \frac{kG(k)T_{11}}{2}\right] \tag{20}$$

where T_i, i = 1,4,7,8,10,11 are the Theodorsen constants. The constants depend on the location of the flap hinge relative to mid chord denoted by c, see figure 5.

The width of the flat plate excluding flaps is denoted B'. In this section two lengths of flaps are investigated, namely with lengths $0.15B'$ (short flaps) and $0.25B'$ (long flaps). The lengths of the flaps and the corresponding c values are shown in figure 5. The Theodorsen constants are shown in table I for long and short flaps.

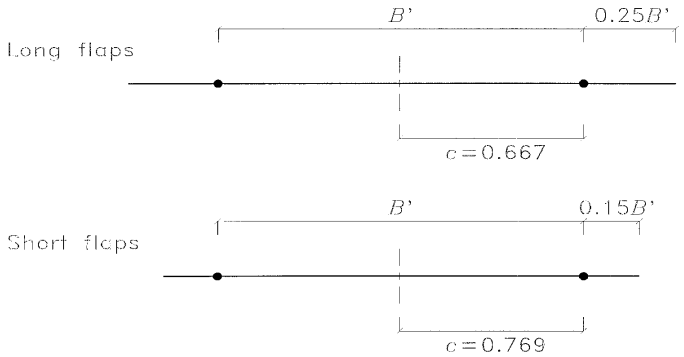

Figure 5. Different lengths of flaps investigated.

Constant	Long flaps	Short flaps
c	0.667	0.769
T_1	−0.0475	−0.019
T_4	−0.344	−0.202
T_7	0.011	0.006
T_8	0.091	0.068
T_{10}	1.586	1.333
T_{11}	0.712	0.414

Table I. Theodorsen constants for long and short flaps.

The additional aerodynamic derivatives are shown in figure 6 and figure 7 for long and short flaps. The forces and moments introduced due to movement of the trailing flap are generally bigger for the long flaps than for the short flaps.

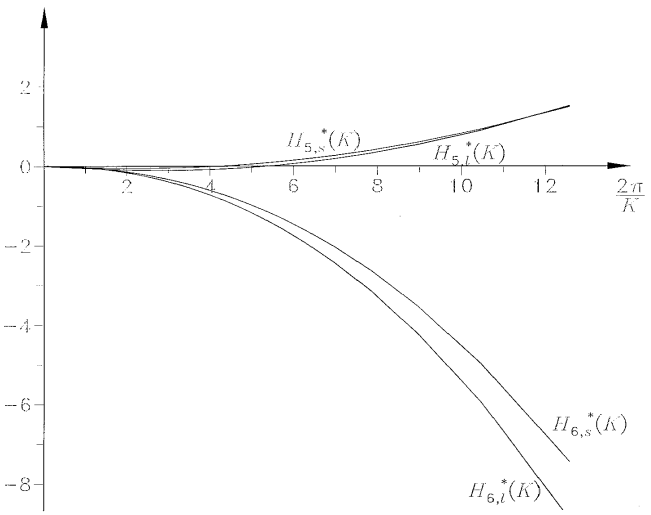

Figure 6. Aerodynamic derivatives for force on flat plate due to movement of trailing flap. Indices *l* and *s* denote long and short flap, respectively.

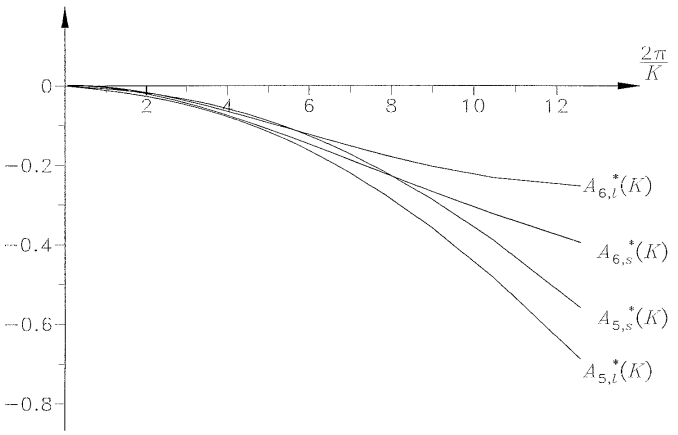

Figure 7. Aerodynamic derivatives for moment on flat plate due to movement of trailing flap. Indices *l* and *s* denote long and short flap, respectively.

2.1.3 *Loads due to Movement of Leading Flap*

Theodorsen's theory for a flat plate is extended to include a leading flap by assuming that the angle of the leading flap has no effect on the circulation. It can be shown that loads due to movement of a leading flap on a thin airfoil in incompressible flow are linear in the angle of the leading flap al and the first and second derivatives. Assuming the leading flap is moved at the same frequency w as the bridge deck and the trailing flap, the motion-induced forces due to movement of the leading flap can be expressed by additional aerodynamic derivatives.

$$F_{al}^P = \frac{1}{2}\rho U^2 B\left[KH_7^\star(K)\frac{B\dot{\alpha}_l}{U} + K^2 H_8^\star(K)\alpha_l\right] \tag{21}$$

$$F_{al}^M = \frac{1}{2}\rho U^2 B^2\left[KA_7^\star(K)\frac{B\dot{\alpha}_l}{U} + K^2 A_8^\star(K)\alpha_l\right] \tag{22}$$

where $H_7^*(K)$, $H_8^*(K)$, $A_7^*(K)$ and $A_8^*(K)$ are aerodynamic derivatives. For a flat

plate with a leading flap the derivatives are

$$H_7^\star(K) = \frac{T_4}{4k} \tag{23}$$

$$H_8^\star(K) = -\frac{T_1}{4} \tag{24}$$

$$A_7^\star(K) = -\frac{1}{8k}\left[T_1 - T_8 - cT_4\right] \tag{25}$$

$$A_8^\star(K) = \frac{1}{8k^2}\left[-T_4 - k^2(T_7 + cT_1)\right] \tag{26}$$

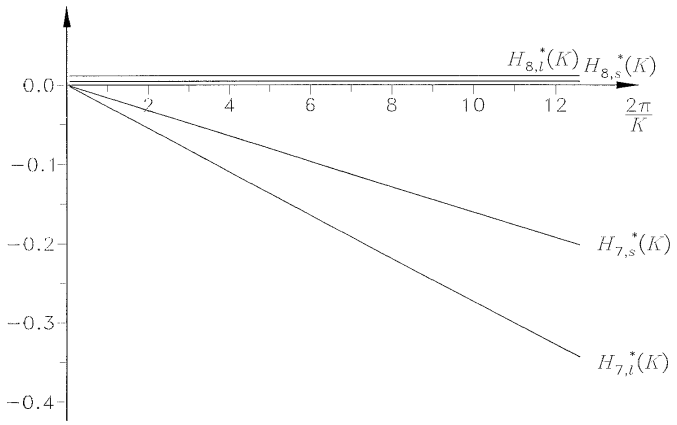

Figure 8. Aerodynamic derivatives for force on flat plate due to movement of leading flap. Indices *l* and *s* denote long and short flap, respectively.

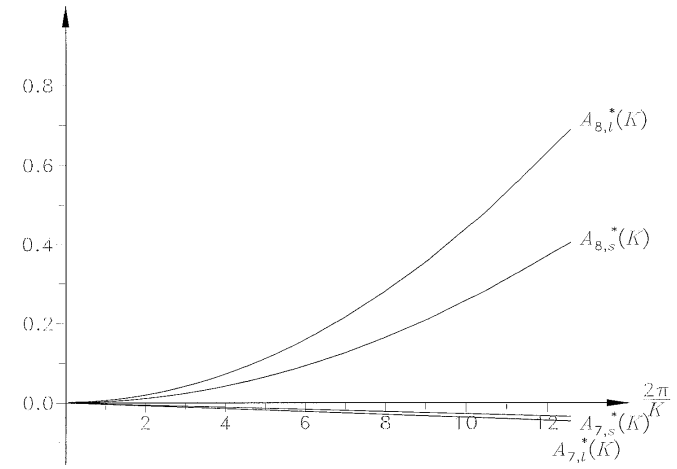

Figure 9. Aerodynamic derivatives for moment on flat plate due to movement of leading flap. Indices *l* and *s* denote long and short flap, respectively.

The additional aerodynamic derivatives for short and long flaps are shown in figures 8 and 9. As for the trailing flap, the forces and moments due to movement of the leading flap are bigger for long flaps than for short flaps. By comparing figures 6 with 8 and 7 with 9 it is seen that turning the trailing flap is more efficient than turning the leading flap the angle $\alpha_l = -\alpha_t$. This is due to the effect of the trailing flap on the circulation.

2.2 Estimation of the flutter wind velocity

As described in section 2.1 two types of flutter are investigated, namely single-degree flutter in torsion and binary flutter. In this section the estimated flutter wind velocity for the two flutter types by using Theodorsen's method are shown for a bridge section with leading and trailing flaps. The angles of the leading flap al and the trailing flap at are expressed in terms of the torsional angle a of the bridge section.

$$\alpha_l(t) = a_l e^{-i\varphi_l}\alpha(t) \tag{27}$$

$$\alpha_t(t) = a_t e^{-i\varphi_t}\alpha(t) \tag{28}$$

where φ_l and φ_t are the phase angles between the flaps and the torsional angle and a_l and a_t are the flap amplification factors. A flap amplification factor is defined as the amplitude of the flap relative to the amplitude of the torsional motion. In the following, a flap configuration refers to fixed parameters a_l, a_t, φ_l and φ_t for the flaps. The results for a bridge section without flaps can be found by setting $a_l \equiv a_t \equiv 0$ in the expressions shown in this section.

2.2.1 *Single-Degree Flutter in Torsion*

In single-degree flutter in torsion the flutter wind velocity U_f is defined as the velocity at which the total damping (structural and aerodynamic) in torsion is zero. The bridge will oscillate at a circular eigenfrequency close to $a_t \equiv 0$; see Dowell et al. [14]. The total damping is zero for

$$A_2^{\star'}(K) = \frac{4I\zeta_\alpha}{\rho B^4} \tag{29}$$

where

$$\begin{aligned} A_2^{\star'}(K) \;=\; & A_2^\star(K) + A_5^\star(K)a_t\cos(-\varphi_t) + A_6^\star(K)a_t\sin(-\varphi_t) + \\ & A_7^\star(K)a_l\cos(-\varphi_l) + A_8^\star(K)a_l\sin(-\varphi_l) \end{aligned} \tag{30}$$

For a flap configuration the flutter wind velocity is

$$U_f \simeq \frac{B\omega_\alpha}{K_f} \tag{31}$$

where K_f is the largest value of K (corresponding to the smallest value of U) for which equation (29) is true. For a flat plate without flaps the flutter condition yields

$$A_2^\star(K) = \frac{4I\zeta_\alpha}{\rho B^4} \tag{32}$$

where $A_2^*(K)$ is negative, see figure 4. Thereby a flat plate will not perform single-degree flutter in torsion.

2.2.2 *Binary Flutter*

In binary flutter the oscillations of the bridge in both vertical and torsional directions will become harmonic at the circular eigenfrequency ω_f at a critical wind velocity U_f. Thereby the structural dissipated energy in the period $T_f = 2\pi/\omega_f$ will be equal to the energy input of the motion-induced wind load, see Dyrbye & Hansen [10].

The circular flutter eigenfrequency ω_f is between the circular eigen-frequencies for the bridge section in bending and torsion, i.e. $\omega_z \leq \omega_f \leq \omega_\alpha$.

The binary flutter condition is

$$\boldsymbol{x}(t) = \boldsymbol{x}_0 e^{i\omega_f t} \tag{33}$$

where

$$\boldsymbol{x}(t) = \begin{bmatrix} z(t) \\ \alpha(t) \end{bmatrix} \tag{34}$$

$$\boldsymbol{x}_0 = \begin{bmatrix} z_0 \\ \alpha_0 e^{-i\varphi_\alpha} \end{bmatrix} \tag{35}$$

where z_0 and α_0 are the amplitudes of the vertical and torsional motion, respectively, and φ_α is the phase angle between the vertical and torsional motion. By inserting the flutter condition in the matrix equation of motion the flutter point can be found graphically by the method described by Dowell et al.[14]. For a number of values of the reduced frequency K the values $X_r(K)$ and $X_i(K)$ are calculated as solutions to the following equations:

$$\begin{aligned}
&A_r(X_r(K),K)X_r^4(K) = \\
&\quad X_r^4(K)\left[mI + \frac{1}{2}\rho B^4 m A_3^{\star'}(K) + \frac{1}{2}\rho B^2 I H_4^\star(K) + \frac{1}{4}\rho^2 B^6\left(-H_1^\star(K)A_2^{\star'}(K)\right.\right. \\
&\quad \left.\left. + H_4^\star(K)A_3^{\star'}(K) + H_2^{\star'}(K)A_1^\star(K) - H_3^{\star'}(K)A_4^\star(K)\right)\right] + \\
&\quad X_r^3(K)\left[\rho B^4 m\zeta_z A_2^{\star'}(K) + \rho B^2 I\zeta_\alpha\frac{\omega_\alpha}{\omega_z}H_1^\star(K)\right] + \\
&\quad X_r^2(K)\left[-mI\frac{\omega_\alpha^2}{\omega_z^2} - mI4\zeta_z\zeta_\alpha\frac{\omega_\alpha}{\omega_z} - mI - \frac{1}{2}\rho B^4 m A_3^{\star'}(K) - \frac{1}{2}\rho B^2 I\frac{\omega_\alpha^2}{\omega_z^2}H_4^\star(K)\right] + \\
&\quad mI\frac{\omega_\alpha^2}{\omega_z^2} = 0
\end{aligned} \tag{36}$$

$$\begin{aligned}
&A_i(X_i(K),K)X_i^3(K) = \\
&\quad X_i^3(K)\left[\frac{1}{2}\rho B^4 m A_2^{\star'}(K) + \frac{1}{2}\rho B^2 I H_1^\star(K) + \frac{1}{4}\rho^2 B^6\left(H_1^\star(K)A_3^{\star'}(K)\right.\right. \\
&\quad \left.\left. + H_4^\star(K)A_2^{\star'}(K) - H_2^{\star'}(K)A_4^\star(K) - H_3^{\star'}(K)A_1^\star(K)\right)\right] + \\
&\quad X_i^2(K)\left[-mI2\zeta_\alpha\frac{\omega_\alpha}{\omega_z} - mI2\zeta_z - \rho B^4 m\zeta_z A_3^{\star'}(K) + \rho B^2 I\zeta_\alpha\frac{\omega_\alpha}{\omega_z}H_4^\star(K)\right] + \\
&\quad X_i(K)\left[-\frac{1}{2}\rho B^4 m A_2^{\star'}(K) - \frac{1}{2}\rho B^2 I\frac{\omega_\alpha^2}{\omega_z^2}H_1^\star(K)\right] + \\
&\quad mI2\zeta_z\frac{\omega_\alpha^2}{\omega_z^2} + mI2\zeta_\alpha\frac{\omega_\alpha}{\omega_z} = 0
\end{aligned} \tag{37}$$

where

$$\begin{aligned}
H_2^{\star'}(K) \;=\; & H_2^\star(K) + H_5^\star(K)a_t\cos(-\varphi_t) + H_6^\star(K)a_t\sin(-\varphi_t) + \\
& H_7^\star(K)a_l\cos(-\varphi_l) + H_8^\star(K)a_l\sin(-\varphi_l)
\end{aligned} \tag{38}$$

$$H_3^{\star\prime}(K) = H_3^{\star}(K) - H_5^{\star}(K)a_t \sin(-\varphi_t) + H_6^{\star}(K)a_t \cos(-\varphi_t) - H_7^{\star}(K)a_l \sin(-\varphi_l) + H_8^{\star}(K)a_l \cos(-\varphi_l) \quad (39)$$

$$A_2^{\star\prime}(K) = A_2^{\star}(K) + A_5^{\star}(K)a_t \cos(-\varphi_t) + A_6^{\star}(K)a_t \sin(-\varphi_t) + A_7^{\star}(K)a_l \cos(-\varphi_l) + A_8^{\star}(K)a_l \sin(-\varphi_l) \quad (40)$$

$$A_3^{\star\prime}(K) = A_3^{\star}(K) - A_5^{\star}(K)a_t \sin(-\varphi_t) + A_6^{\star}(K)a_t \cos(-\varphi_t) - A_7^{\star}(K)a_l \sin(-\varphi_l) + A_8^{\star}(K)a_l \cos(-\varphi_l) \quad (41)$$

The flutter point (X_f, K_f) is the point where the solution curves $X_r(K)$ and $X_i(K)$ cross. The circular flutter frequency ω_f and the flutter wind velocity U_f can be determined by

$$\omega_f = X_f \omega_z \quad (42)$$

$$U_f = \frac{B\omega_f}{K_f} \quad (43)$$

When there is more than one intersection of the solution curves, the flutter point corresponds to the intersection point with the largest value of K (corresponding to the smallest value of U). The factor $\frac{\alpha_0}{z_0}e^{-i\varphi_\alpha}$ defined by equations (33) and (35) can be calculated by inserting the values ω_f and K_f into the matrix equation of motion with the flutter condition. The phase angle φ_α between the vertical and torsional motion is

$$\varphi_\alpha = -\tan^{-1}\left(\frac{\mathrm{Im}\left(\frac{\alpha_0}{z_0}e^{-i\varphi_\alpha}\right)}{\mathrm{Re}\left(\frac{\alpha_0}{z_0}e^{-i\varphi_\alpha}\right)}\right) \quad (44)$$

As an example, the flutter wind velocity for binary flutter is estimated for the bridge section model used in the wind tunnel experiments. The bridge section model is equipped with long flaps; see the corresponding flat plate in figure 5. The parameters of the model are shown in table II. The aerodynamic derivatives for the model are approximated by the values for a flat plate shown in section 2.1.

Parameter	Symbol	Value
Width of model incl. flaps	B	0.937 m
Mass per unit length	m	17.94 kg/m
Mass moment of inertia per unit length	I	0.589 kg m^2/m
Circular frequency for bending	ω_z	5.2 rad/s
Circular frequency for torsion	ω_α	10.1 rad/s
Structural damping in bending	ζ_z	0.012
Structural damping in torsion	ζ_α	0.008
Mass density of air	ρ	1.28 kg/m^3

Table II. Parameters for bridge section model used in example.

The flutter point is (X_f, K_f) = (1.273, 0.758). The circular flutter frequency ω_f and

flutter wind velocity U_f are

$$\omega_f = X_f \omega_z = 1.273 \cdot 5.2 = 6.62 \text{ rad/s} \tag{45}$$

$$U_f = \frac{B\omega_f}{K_f} = \frac{0.937 \cdot 6.62}{0.758} = 8.18 \text{ m/s} \tag{46}$$

As expected, the circular flutter frequency is between the circular frequencies for bending and torsion, see table II. By using equation (44) the phase angle between the vertical and torsional motion can be calculated

$$\varphi_\alpha = -\tan^{-1}\left(\frac{-1.192}{1.568}\right) = 0.650 \text{ rad} = 37^\circ \tag{47}$$

The flutter wind velocity U_f for binary flutter is calculated for different flap amplification factors al and phase angles CPI for the leading flap. The trailing flap is not moved, i.e. $a_t \equiv 0$. The results are shown in figure 10. The flutter wind velocity is increased when the phase angle for the leading flap φ_l is in the interval $[0.6\pi/6;\ 6.6\pi/6]$, otherwise the flutter wind velocity is decreased. The phase angle for maximum increase of the flutter wind velocity is dependent on the value of the flap amplification factor a_l.

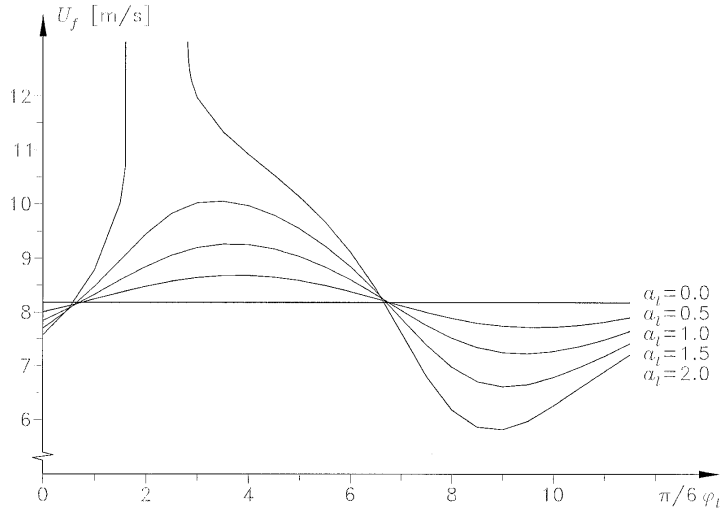

Figure. 10. Flutter wind velocity when only the leading flap is used.

The flutter wind velocity U_f for binary flutter is calculated for different values of a_t and φ_t for the trailing flap. The leading flap is not moved, i.e. $a_l \equiv 0$. The results are shown in figure 11. The interval where the flutter wind velocity is increased, when the trailing flap is moved, is dependent on the flap amplification factor at. The flutter wind velocity is generally decreased when the phase angle of the trailing flap φ_t is in the interval $[\pi/6;\ 6\pi/6]$. For phase angles outside this interval the flutter wind velocity is generally increased. Again the phase angle for maximum increase of the flutter wind velocity is dependent on the value of the flap amplification factor a_t.

By comparing figures 10 and 11 it is seen that the trailing flap is much more efficient than the leading flap. The potential theory used assumes that there is no separation of the flow around the flat plate. This assumption can hardly be met in

practice, therefore it is expected that the effect of the trailing flap is overestimated by the Theodorsen theory for a flat plate. For small values of the flap amplification factors the optimal phase angles are $\varphi_l \approx 3\pi/6$ and $\varphi_t \approx 8\pi/6$. These phase angles are used in figure 12 where movement of both flaps compared to movement of the leading and trailing flap separately is shown. As seen in figure 12 the flutter wind velocity is only slightly increased for flap amplification factors below approximately 0.8 when only one flap is moved. When the trailing flap is moved with a flap amplification factor at above 0.8 the flutter wind velocity is increased considerably and for a_t > 0.95 binary flutter will not occur. By using both flaps, binary flutter will not occur when both flap amplification factors are above approximately 0.6.

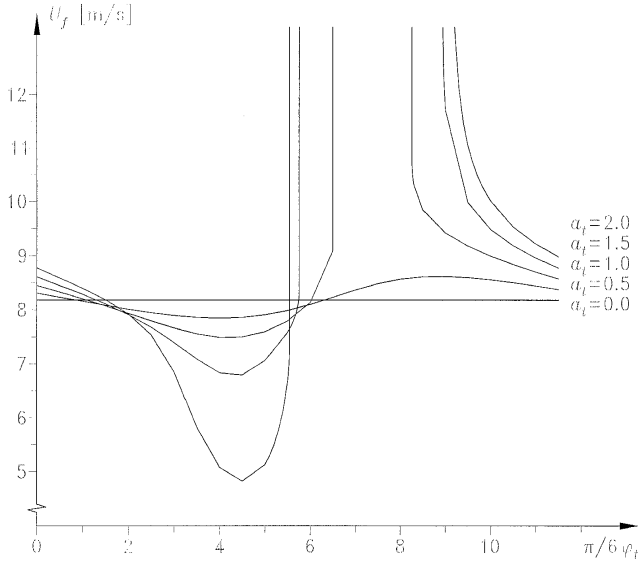

Figure 11. Flutter wind velocity when only the trailing flap is used.

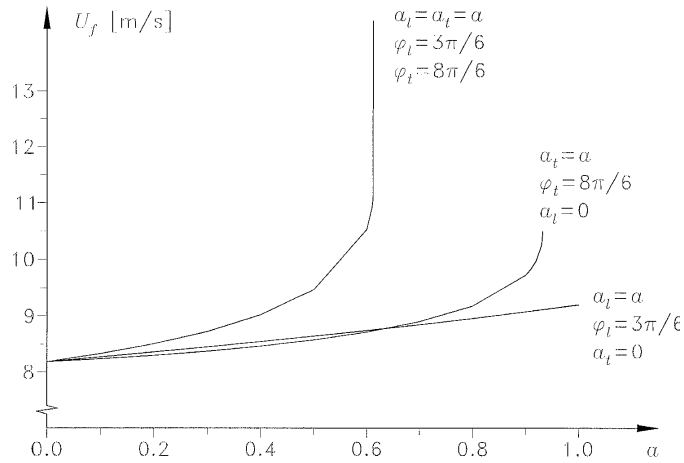

Figure 12. Movement of both flaps compared to movement of the flaps separately.

2.3 Estimation of damping by te AMC method

In the Air Material Command (AMC) method the necessary structural damping of the bridge section for fulfilling the binary flutter condition in equation (33) is plotted against the mean wind velocity; see Fung [15]. Flutter occurs when the necessary structural damping exceeds the actual structural damping of the bridge section. By

using the AMC method the following equation is solved with respect to the complex variable Z

$$Z^2\left[\left(\frac{\omega_z}{\omega_\alpha}\right)^2\right]+Z\left[-1-\left(\frac{\omega_z}{\omega_\alpha}\right)^2-\left(\frac{\omega_z}{\omega_\alpha}\right)^2\frac{\rho B^4}{2I}(A_2^{\star\prime}(K)i+A_3^{\star\prime}(K))-\frac{\rho B^2}{2m}(H_1^\star(K)i+H_4^\star(K))\right]+1+\frac{\rho B^4}{2I}(A_2^{\star\prime}(K)i+A_3^{\star\prime}(K))+\frac{\rho B^2}{2m}(H_1^\star(K)i+H_4^\star(K))+\frac{\rho^2 B^6}{4mI}\Big((H_1^\star(K)i+H_4^\star(K))(A_2^{\star\prime}(K)i+A_3^{\star\prime}(K))-(H_2^{\star\prime}(K)i+H_3^{\star\prime}(K))(A_1^\star(K)i+A_4^\star(K))\Big)=0 \quad (48)$$

For a number of reduced frequencies K_1, K_2,..., equation (48) is solved and corresponding values of the mean wind velocity U and the damping factor g are calculated

$$U(K_i)=\frac{B\omega_\alpha}{K_i\sqrt{\mathrm{Re}(Z(K_i))}} \quad (49)$$

$$g(K_i)=\frac{\mathrm{Im}(Z(K_i))}{\mathrm{Re}(Z(K_i))} \quad (50)$$

The damping factor g is defined as twice the necessary structural damping (for binary flutter. It is assumed that the structural damping is the same for bending and torsion, i.e. $\zeta=\zeta_\alpha=\zeta_z$, The flutter wind velocity U_f is found by

$$g(U_f)=2\zeta \quad (51)$$

As in section 2.2, the bridge section model used in the wind tunnel experiments is used in the example. The parameters for the model are shown in table II and the aerodynamic derivatives for a flat plate are used. The following approximation is made: ζ = 0.01. The results are shown in figure 13 for no movement of the flaps, i.e. a_l = a_t = 0, and for a_l = a_t = 0.6, $\varphi_l=3\pi/6$ and $\varphi_t=8\pi/6$.

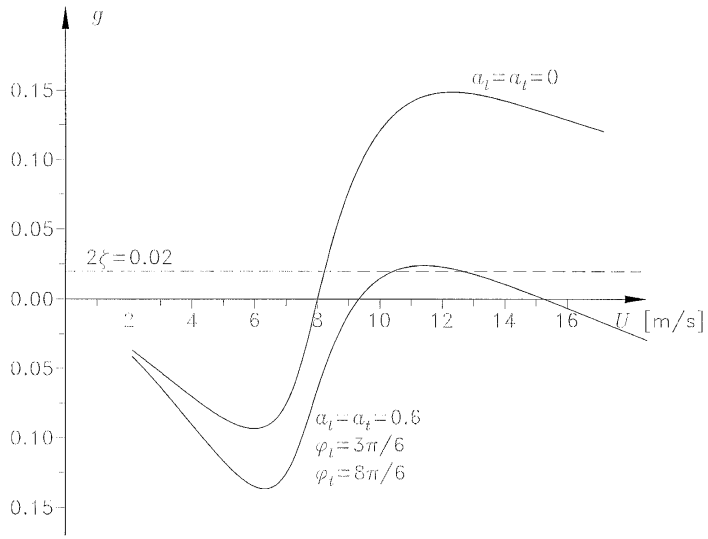

Figure 13. Damping factor as a function of the mean wind velocity.

The flutter wind velocity for the bridge section model is found as the mean wind velocity for which g = 0.02. For no movement of the flaps the flutter wind velocity is

8.22 m/s. This value is very close to the flutter wind velocity found by Theodorsen's method in section 2.2, i.e. 8.18 m/s. If it is assumed that the structural damping ζ is in the interval [0.008; 0.012] corresponding to the structural damping for torsion and bending, respectively, then the flutter wind velocity is in the interval [8.18; 8.27] m/s, which agrees very well with the flutter wind velocity found by Theodorsen's method. When both flaps are moved using $a_l = a_t = 0.6$ and the phase angles found in section 2.2, i.e. $\varphi_l = 3\pi/6$ and $\varphi_t = 8\pi/6$, then the flutter wind velocity is increased to 10.43 m/s in the interval [10.08, 11.24] m/s. Again, this flutter wind velocity agrees very well with the flutter wind velocity of 10.53 m/s for this flap configuration found by the Theodorsen method.

3. ACTIVE CONTROL SYSTEMS

In active structural control the motion of the structure is controlled by means of the action of a control system through some external energy supply. The basic active control configuration consists of:

- Sensors located on or in the structure to measure excitation and/or structural response variables.
- Devices to process the measurements and to compute the control action based on a control algorithm.
- Actuators to make the control action.

When the motion of the bridge is measured and used to calculate the flap positions (i.e. the control action), the control configuration is referred to as closed-loop control. The effect of closed-loop control is to modify the structural parameters (stiffness and damping) so that the bridge responds more favour ably to the excitation. When the wind velocity (i.e. the excitation) is measured and used to control the bridge the control configuration is referred to as open-loop control. The effect of the open-loop component is a modification of the excitation. In closed-open-loop control the flap positions are calculated based on both the measured motion of the bridge and the measured wind velocity.

Three methods of computing the flap positions are described:

- Classical linear optimal closed-loop control, see section 3.1.
- Instantaneous optimal closed-loop control, see section 3.2.
- Closed-loop control with constant phase angles between the motion of the flaps and the torsional motion of the bridge, see section 3.3.

Classical linear optimal closed-open-loop and open-loop control are generally not feasible in structural control applications since for this type of control the excitation must be known a priori during the control interval; see Soong [16]. For instantaneous optimal control it is possible to derive the open-loop and closed-open-loop control laws; see Soong [16]. But these control laws that contain information about the excitation term are much more complicated than the closed-loop control law.

3.1 Classical linear optimal Closed-Loop Control

In structural control applications of classical linear optimal control the usually studied performance index J to be minimized in the control interval $[0; t_f]$ can be written as follows; see Soong [16]

$$J = \int_0^{t_f} \left[\boldsymbol{y}^T(t)\boldsymbol{Q}\boldsymbol{y}(t) + \boldsymbol{u}^T(t)\boldsymbol{R}\boldsymbol{u}(t) \right] dt \tag{52}$$

where the vectors ***y*** and ***u*** are composed of the structural parameters and the control actions, respectively.

$$\boldsymbol{y}(t) = \begin{bmatrix} z(t) \\ \alpha(t) \\ \dot{z}(t) \\ \dot{\alpha}(t) \end{bmatrix} \tag{53}$$

$$\boldsymbol{u}(t) = \begin{bmatrix} \alpha_t(t) \\ \alpha_l(t) \end{bmatrix} \tag{54}$$

Q and ***R*** are weighting matrices, where the elements are selected to achieve the desired connection between the control effectiveness and the control energy consumption. I.e. large values of the elements in ***Q*** compared to the elements in ***R*** indicate that the reduction of the motion of the model is more important than the energy required turning the flaps. The following weighting matrices are used by Wu et al.[18].

$$\boldsymbol{Q} = \begin{bmatrix} \boldsymbol{K}_s & \boldsymbol{0} \\ \boldsymbol{0} & \boldsymbol{M}_s \end{bmatrix} \tag{55}$$

$$\boldsymbol{R} = \beta \boldsymbol{I} \tag{56}$$

where $\boldsymbol{M_s}$ and $\boldsymbol{K_s}$ are the mass and stiffness matrices, respectively. ***I*** is the identity matrix. The factor β is the relative importance of the control effectiveness compared to the control energy consumption. For the uncontrolled case, $\beta = \infty$.

The linear optimal closed-loop control law is e.g. derived by Soong [16].

$$\boldsymbol{u}(t) = \boldsymbol{G}^{lo}(t)\boldsymbol{y}(t) \tag{57}$$

where the control gain matrix $\boldsymbol{G}^{lo}(t)$ is given by

$$\boldsymbol{G}^{lo}(t) = -\frac{1}{2}\boldsymbol{R}^{-1}\boldsymbol{B}^T\boldsymbol{P}(t) \tag{58}$$

The Riccatti matrix ***P***(*t*) is found by solving the Riccatti equation

$$\dot{\boldsymbol{P}}(t) + \boldsymbol{P}(t)\boldsymbol{A} - \frac{1}{2}\boldsymbol{P}(t)\boldsymbol{B}\boldsymbol{R}^{-1}\boldsymbol{B}^T\boldsymbol{P}(t) + \boldsymbol{A}^T\boldsymbol{P}(t) + 2\boldsymbol{Q} = 0, \quad \boldsymbol{P}(t_f) = \boldsymbol{0} \tag{59}$$

The elements in the Riccatti matrix are constant during most of the control interval dropping to zero near the end of the control interval, i.e. near t_f. Therefore, the time-dependent Riccatti matrix is approximated by the constant matrix ***P*** corresponding to the values in the first part of the control interval.

Then the control gain matrix is

$$\boldsymbol{G}^{lo} = -\frac{1}{2}\boldsymbol{R}^{-1}\boldsymbol{B}^T\boldsymbol{P} \tag{60}$$

As an example, the gain matrix $\boldsymbol{G}^{lo}$ is calculated for the bridge section model used in the wind tunnel experiments for β = 10 and β = 100. The parameters of the

model are shown in table II. The aerodynamic derivatives for the model are approximated by the values for a flat plate shown in section 2.1. It is assumed that the model performs binary flutter with ω_f = 6.62 rad/s and U_f = 8.18 m/s, see equations (45) and (46).

$$\beta = 10 \quad \Rightarrow \quad \boldsymbol{G}_{10}^{lo} = \begin{bmatrix} 2.89 & 0.91 & 1.76 & 0.09 \\ 0.73 & -0.28 & 0.22 & -0.30 \end{bmatrix} \tag{61}$$

$$\beta = 100 \quad \Rightarrow \quad \boldsymbol{G}_{100}^{lo} = \begin{bmatrix} 0.34 & 0.17 & 0.57 & 0.04 \\ 0.10 & -0.03 & 0.01 & -0.08 \end{bmatrix} \tag{62}$$

As expected, the elements of the gain matrix are reduced when the β-value is increased.

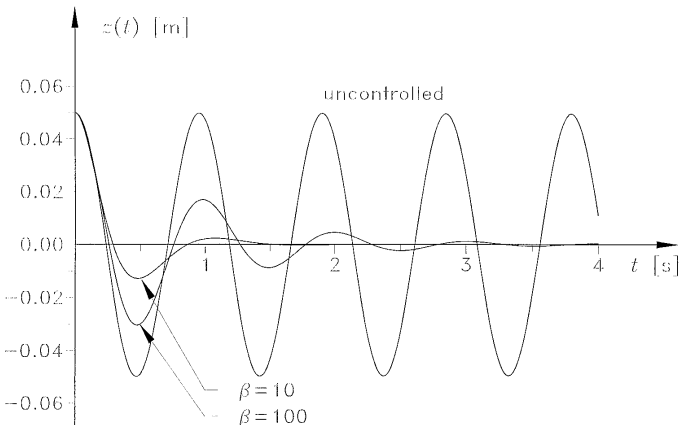

Figure 14. Uncontrolled and controlled vertical motion for β = 10 and β = 100 using classical linear optimal control.

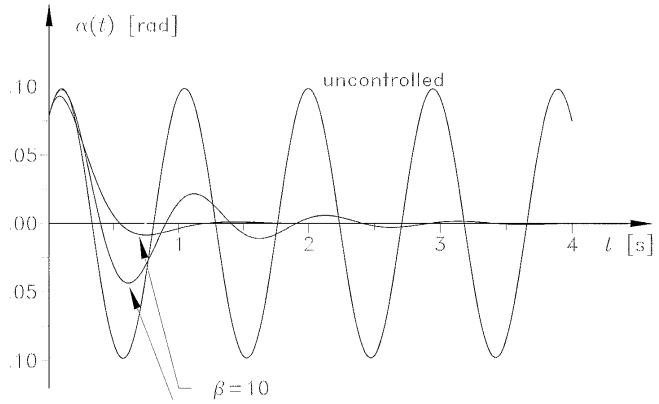

Figure 15. Uncontrolled and controlled torsional motion for β = 10 and β = 100 using classical linear optimal control.

The vertical and torsional uncontrolled motion and controlled motion with β = 10 and β = 100 are shown in figures 14 and 15, respectively. Both the vertical and torsional oscillations are reduced very fast, especially for β = 10.

The movements of the trailing and leading flap are shown in figure 16 for β = 10 and in figure 17 for β = 100. The maximum flap angle for β = 10 is about 16° and for β = 100 the maximum angle is about 8°. For both β-values the trailing flap is turned more than the leading flap and there is a phase angle between the motion of the

trailing flap and the leading flap.

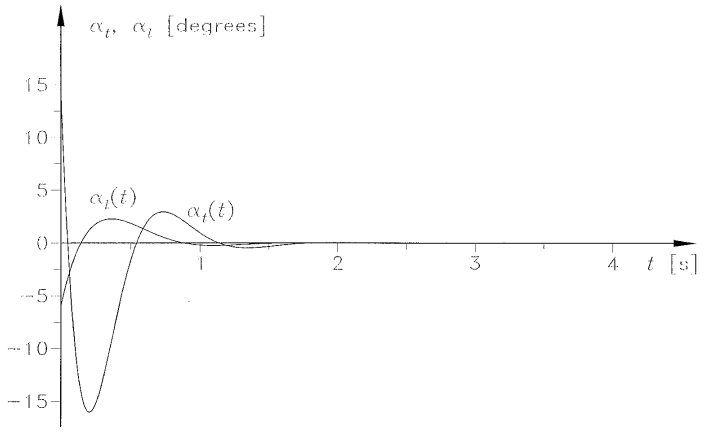

Figure 16. Flap angles for β = 10 using classical linear optimal control.

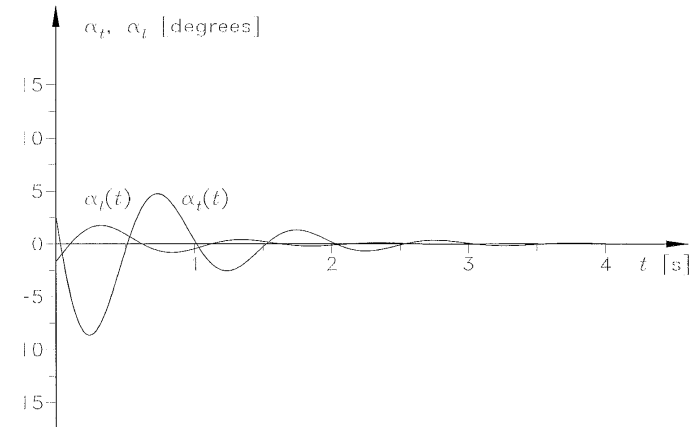

Figure 17. Flap angles for β = 100 using classical linear optimal control.

3.2 Instantaneous optimal Closed-Loop Control

In instantaneous optimal control a time-dependent performance index $J(t)$ is defined by e.g.

$$J(t) = \boldsymbol{y}^T(t)\boldsymbol{Q}\boldsymbol{y}(t) + \boldsymbol{u}^T(t)\boldsymbol{R}\boldsymbol{u}(t) \tag{63}$$

This performance index is minimized at every time instant t during the control interval, i.e. for all $0 \le t \le t_f$; see Soong [16].

In instantaneous optimal closed-loop control the control law is

$$\boldsymbol{u}(t) = \boldsymbol{G}^{io}\boldsymbol{y}(t) \tag{64}$$

The control gain matrix is

$$\boldsymbol{G}^{io} = -\frac{\Delta t}{2}\boldsymbol{R}^{-1}\boldsymbol{B}^T\boldsymbol{Q} \tag{65}$$

where Δt is a small time interval; see Soong [16]. By comparing the gain matrices $\boldsymbol{G}^{lo}$ and $\boldsymbol{G}^{io}$ for linear optimal and instantaneous optimal closed-loop control it is seen that the Riccatti matrix $\boldsymbol{P}$ in equation (60) is replaced by $\Delta t\boldsymbol{Q}$ in equation (65). The instantaneous control law is thus much simpler than the linear optimal control law because solving the Riccatti matrix is omitted.

The control gain matrix is calculated for the example described in section 3.1 for (3 = 2 and (3 = 10. The weighting matrices in equations (55) and (56) for classical linear optimal control are used

$$\beta = 2 \quad \Rightarrow \quad \boldsymbol{G}_2^{io} = \begin{bmatrix} 0.000 & 0.000 & 1.230 & 0.060 \\ 0.000 & 0.000 & -0.004 & -0.098 \end{bmatrix} \tag{66}$$

$$\beta = 10 \quad \Rightarrow \quad \boldsymbol{G}_{10}^{io} = \begin{bmatrix} 0.000 & 0.000 & 0.246 & 0.012 \\ 0.000 & 0.000 & -0.001 & -0.020 \end{bmatrix} \tag{67}$$

When β is multiplied by a factor a, $\boldsymbol{G}$ is multiplied by l/α, as $\boldsymbol{R}^{-1} = 1/\beta \boldsymbol{I}$. The flap angles only depend on the vertical and torsional velocities for the current selection of weighting matrices $\boldsymbol{R}$ and $\boldsymbol{Q}$.

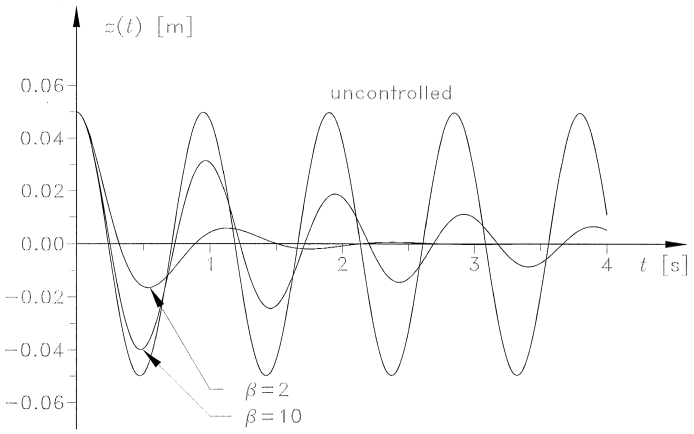

Figure 18. Uncontrolled and controlled vertical motion for β = 2 and β = 10 using instantaneous optimal control.

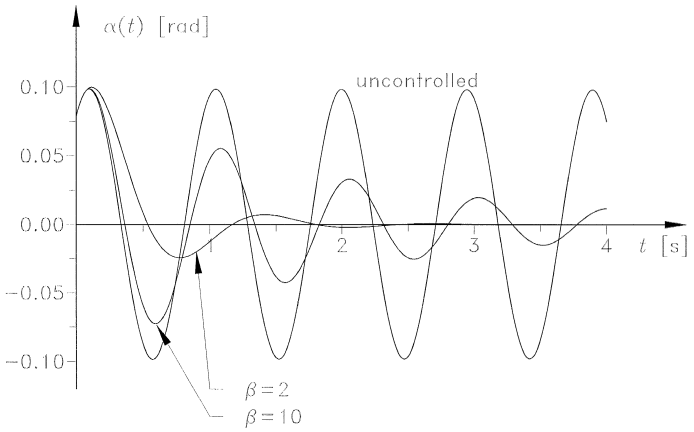

Figure 19. Uncontrolled and controlled torsional motion for β = 2 and β = 10 using instantaneous optimal control.

The vertically and torsionally uncontrolled motion and controlled motion with β = 2 and β = 10 are shown in figures 18 and 19, respectively. Both the vertical and torsional oscillations are reduced very fast, especially for β = 2.

The movements of the trailing and leading flap are shown in figure 20 for β = 2. The flap angles shown in figure 20 can be compared with the flap angles shown in

figure 16, where classical linear optimal control is used. The shapes of the flap angle curves are much alike, but the flaps are slightly delayed in instantaneous control compared to classical linear optimal control.

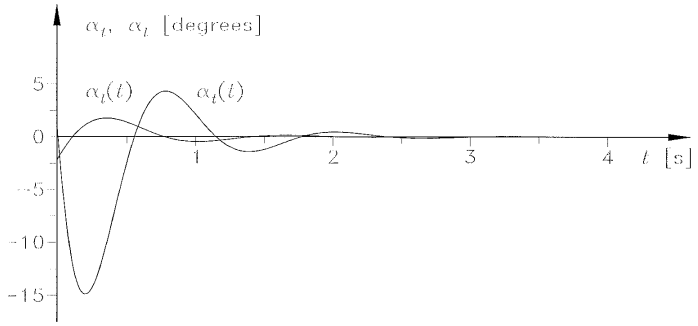

Figure 20. Flap angles for β = 2 using instantaneous optimal control.

3.3 Constant phase angle

As described in section 2.2.2, binary flutter occurs when the structural dissipated energy E_{dis} is equal to the energy input E_{input} from the motion-induced wind load during a period. The binary flutter condition is

$$\begin{bmatrix} z(t) \\ \alpha(t) \end{bmatrix} = \begin{bmatrix} z_0 \cos(\omega_f t) \\ \alpha_0 \cos(\omega_f t - \varphi_\alpha) \end{bmatrix} \tag{68}$$

where z_0 and α_0 are the amplitudes of the vertical and torsional oscillations and φ_α is the phase angle between the vertical and torsional oscillation.

The structural dissipated energy per metre during the period $T_f = 2\pi / \omega_f$ is

$$\begin{aligned} E_{dis} &= \int_0^{T_f} \left[m2\zeta_z\omega_z \frac{dz(t)}{dt} + I2\zeta_\alpha\omega_\alpha \frac{d\alpha(t)}{dt} \right] dt \\ &= \frac{K_f U_f}{B} 2\pi \left(m\zeta_z\omega_z z_0^2 + I\zeta_\alpha\omega_\alpha\alpha_0^2 \right) \end{aligned} \tag{69}$$

The energy input per metre during the period T_f for no regulation of the flaps is

$$\begin{aligned} E_{input} &= \int_0^{T_f} \left[F_{ad}^P(t) \frac{dz(t)}{dt} + F_{ad}^M(t) \frac{d\alpha(t)}{dt} \right] dt \\ &= \frac{1}{2}\rho U_f^2 B K_f^2 \pi z_0 \alpha_0 \left[\frac{z_0}{B\alpha_0} H_1^\star(K_f) + \frac{B\alpha_0}{z_0} A_2^\star(K_f) + \right. \\ &\quad \left. (H_2^\star(K_f) + A_1^\star(K_f)) \cos(-\varphi_\alpha) + (H_3^\star(K_f) - A_4^\star(K_f)) \sin(-\varphi_\alpha) \right] \end{aligned} \tag{70}$$

As both the oscillations and the motion-induced wind load have sine-shape, this shape is also selected for the control action and thereby the flap angles.

$$\begin{bmatrix} \alpha_t(t) \\ \alpha_l(t) \end{bmatrix} = \begin{bmatrix} \alpha_{t0} \cos(\omega_f t - \varphi_\alpha - \varphi_t) \\ \alpha_{l0} \cos(\omega_f t - \varphi_\alpha - \varphi_l) \end{bmatrix} \tag{71}$$

where α_{t0} and α_{l0} are the amplitudes of the flap angles and ω_z and φ_l are the phase angles between the torsional oscillation and the flap oscillations.

The additional energy input per metre $\Delta E_{input,t}$ and $\Delta E_{input,l}$ during the period T_f for regulation of the trailing and leading flap, respectively, is

$$\begin{aligned}\Delta E_{input,t} &= \int_0^{T_f}\left[F_{at}^P(t)\frac{dz(t)}{dt}+F_{at}^M(t)\frac{d\alpha(t)}{dt}\right]dt \\ &= \frac{1}{2}\rho U_f^2 B K_f^2 \pi z_0 \alpha_0\left(\frac{\alpha_{t0}}{\alpha_0}\left[H_5^\star(K_f)\cos(-\varphi_\alpha-\varphi_t)+H_6^\star(K_f)\sin(-\varphi_\alpha-\varphi_t)\right]+\right. \\ &\quad \left.\frac{B\alpha_{t0}}{z_0}\left[A_5^\star(K_f)\cos(-\varphi_t)+A_6^\star(K_f)\sin(-\varphi_t)\right]\right) \qquad (72)\end{aligned}$$

$$\begin{aligned}\Delta E_{input,l} &= \int_0^{T_f}\left[F_{al}^P(t)\frac{dz(t)}{dt}+F_{al}^M(t)\frac{d\alpha(t)}{dt}\right]dt \\ &= \frac{1}{2}\rho U_f^2 B K_f^2 \pi z_0 \alpha_0\left(\frac{\alpha_{l0}}{\alpha_0}\left[H_7^\star(K_f)\cos(-\varphi_\alpha-\varphi_l)+H_8^\star(K_f)\sin(-\varphi_\alpha-\varphi_l)\right]+\right. \\ &\quad \left.\frac{B\alpha_{t0}}{z_0}\left[A_7^\star(K_f)\cos(-\varphi_l)+A_8^\star(K_f)\sin(-\varphi_l)\right]\right) \qquad (73)\end{aligned}$$

The flap configuration parameters α_{t0}, α_{l0}, φ_t and φ_l can be selected so the energy input is reduced. The optimal phase angles are found for

$$\frac{d(\Delta E_{input,t})}{d\varphi_t}=0 \quad \Rightarrow$$

$$\varphi_t=-\tan^{-1}\left(\frac{-z_0H_5^\star(K_f)\sin(-\varphi_\alpha)+z_0H_6^\star(K_f)\cos(-\varphi_\alpha)+B\alpha_0A_6^\star(K_f)}{z_0H_5^\star(K_f)\cos(-\varphi_\alpha)+z_0H_6^\star(K_f)\sin(-\varphi_\alpha)+B\alpha_0A_5^\star(K_f)}\right) \qquad (74)$$

$$\frac{d(\Delta E_{input,l})}{d\varphi_l}=0 \quad \Rightarrow$$

$$\varphi_l=-\tan^{-1}\left(\frac{-z_0H_7^\star(K_f)\sin(-\varphi_\alpha)+z_0H_8^\star(K_f)\cos(-\varphi_\alpha)+B\alpha_0A_8^\star(K_f)}{z_0H_7^\star(K_f)\cos(-\varphi_\alpha)+z_0H_8^\star(K_f)\sin(-\varphi_\alpha)+B\alpha_0A_7^\star(K_f)}\right) \qquad (75)$$

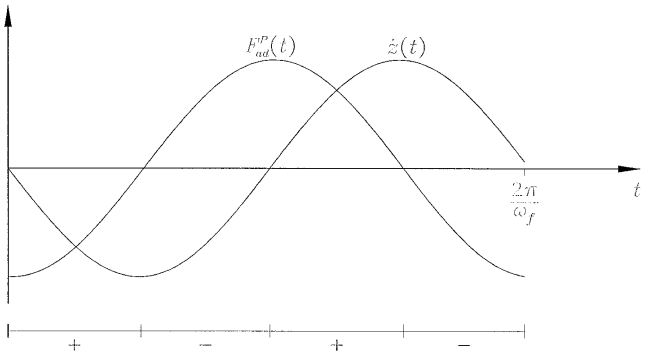

Figure 21. Sign of contribution to energy extracted from force of motion-induced wind load.

For the example described in section 3.1 the force of the motion-induced wind load $F_{ad}^P(t)$ and the vertical velocity $\dot{z}(t)$ are shown in figure 21. The moment of the motion-induced wind load $F_{ad}^M(t)$ and the torsional velocity $\dot{\alpha}(t)$ are shown in figure 22. The time intervals with positive contribution to E_{input} are marked with "+" in figures 21 and 22. The time intervals with negative contribution to E_{input} are marked

with "-". The dissipated structural energy and the energy input are $E_{dis} = E_{input} = 0.136$ Nm/m.

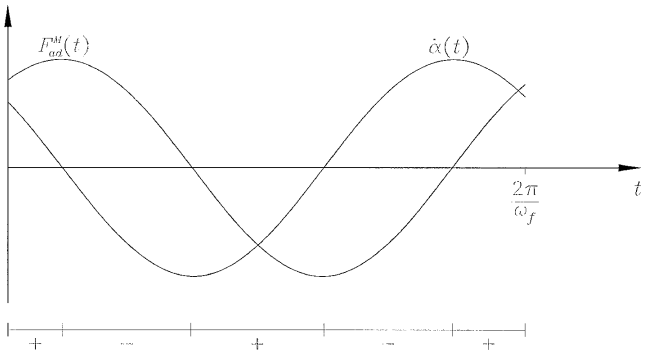

Figure 22. Sign of contribution to energy extracted from moment of motion-induced wind load.

The additional energy input per metre $\Delta E_{input,t}$ and $\Delta E_{input,l}$ during the period T_f is dependent on φ_t and φ_l, respectively, see figures 23 and 24. The optimal flap angles and maximum contribution to energy input per metre are

$$\varphi_{t,opt} = 7.91 \cdot \frac{\pi}{6} = 237^\circ \quad \Rightarrow \quad \min(\Delta E_{input,t}(\varphi_t)) = -12.68\alpha_{t0} \text{ Nm/m} \qquad (76)$$

$$\varphi_{l,opt} = 2.02 \cdot \frac{\pi}{6} = 61^\circ \quad \Rightarrow \quad \min(\Delta E_{input,l}(\varphi_l)) = -1.786\alpha_{t0} \text{ Nm/m} \qquad (77)$$

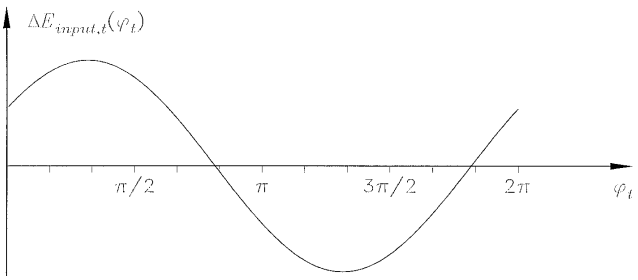

Figure 23. Energy input due to movement of trailing flap.

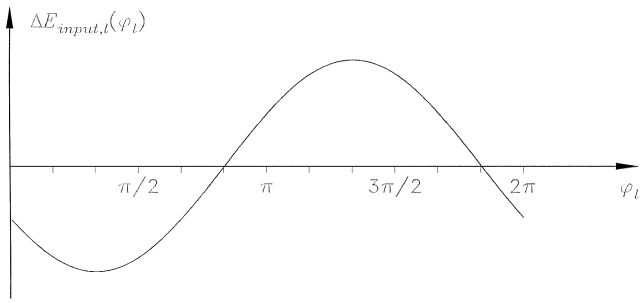

Figure 24. Energy input due to movement of leading flap.

For flap angle amplitudes equal to the amplitude of the torsional motion, i.e. $\alpha_{t0} = \alpha_{l0} = \alpha_0 = 0.098$ the total energy input is

$$E_{input} + \Delta E_{input,t}(\varphi_{t,opt}) + \Delta E_{input,l}(\varphi_{l,opt}) = 0.136 - 1.243 - 0.175 = -1.282 \text{ Nm/m} \quad (78)$$

As seen the effect of the trailing flap is about seven times the effect of the leading flap. The flap configuration described decreases the energy extracted from the wind, so binary flutter will not occur for the investigated wind velocity.

4. WIND TUNNEL EXPERIMENTS

The purpose of the wind tunnel experiments is described in section 4.1. The bridge section model is described in section 4.2. The test programme used during the experiments is described in section 4.3. Examples of results of damping experiments are shown in section 4.4 and estimation of parameters is described in section 4.5. The results of the wind tunnel experiments are compared with the flat plate approximation in section 5.

The bridge section model, suspension system, flap regulation system and the wind tunnel experiments are further described in Hansen [1] and (Hansen et al. [17].

4.1 Purpose of the experiments

The purpose of the experiments with the bridge section model in the wind tunnel is primarily to investigate how the damping of the model is dependent on the flap configuration for increasing wind velocities. These results are compared with the theoretical results for a flat plate by using the Air Material Command (AMC) method described in section 2.3.

The bridge section model is dimensioned to fit into the Wind Tunnel for Building Aerodynamics at the Instituto Superior Tecnico in Lisbon, Portugal, whereby a practically usable model is dimensioned. Further, it is important that the model is realistic compared to a real bridge - but no specific bridge is investigated. Both the trailing flap and the leading flap can be regulated in the model, since the effect of two flaps instead of one is essential. The purpose of the flap in the leading edge is primarily to introduce a load on the bridge opposite to the motion of the bridge. The purpose of the flap in the trailing edge is primarily to change the direction of the wake. The flaps are able to rotate approximately $\pm 20^{o}$ from the horizontal positions. It is of interest to investigate flaps with different lengths. Therefore, flaps with lengths 0.15*B*' and 0.25*B*' are constructed, where *B*' is the width of the bridge section model excluding flaps. During the wind tunnel experiments only the long flaps have been used.

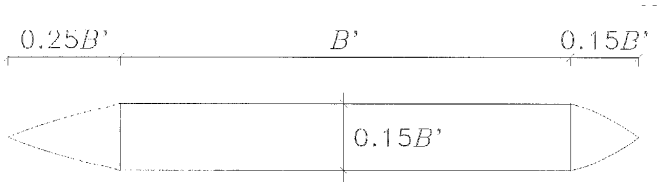

Figure 25. Simplified model of suspension bridge section with flaps.

4.2 Bridge section model

Experiments have shown that the critical wind velocity for a streamlined girder is much higher than for a rectangular girder, see (Ostenfeld & Larsen, 1992). The bridge section model is therefore made streamlined with the flaps as the streamlined part. A simplified model of the bridge section equipped with flaps is illustrated in figure 25. The width of the model excluding flaps is *B*' and the height of the model is 0.15B'. In the experiments two long flaps with the length 0.25*B*' are used. For illustration the model in figure 25 is shown with a long flap at the left hand side and a short flap at the right hand side.

4.3 Test programme

In the experiments the following control algorithm is used to calculate the desired angles $\alpha_t(t)$ and $\alpha_l(t)$ of the trailing and leading flap:

$$\left.\begin{aligned}\alpha_t(t) &= a_t\alpha(t)\\ \alpha_l(t) &= -a_l\alpha(t)\end{aligned}\right\} \tag{79}$$

where is the torsional angle of the model at the time *t*, a_t and a_l are amplitude amplification factors for the trailing and leading flap, respectively. The flaps are started slowly by multiplying the desired positions by a factor t/T_0 when $t < T_0$. The time for slow start is selected equal to T_0 = 1 s. The following experiments are performed:

- The flaps are not regulated, flap configuration 0: $a_t = a_l = 0$.
  - Free vibration (vertical motion, torsional motion, both vertical and torsional motion).
  - Both vertical and torsional motion with the following wind speeds: 2.5 m/s, 4.0 m/s, 5.9 m/s, 7.1 m/s, 7.5 m/s and 8.2 m/s.
- Both flaps are regulated, flap configuration 1: a_t =-6 and a_l =6.
  - Free vibration (torsional motion, both vertical and torsional motion).
  - Both vertical and torsional motion with the following wind speeds: 2.5 m/s, 4.0 m/s, 5.9 m/s, 7.1 m/s and 7.7 m/s.
- Both flaps are regulated, flap configuration 2: a_t = -20 and a_l =20.
  - Free vibration (torsional motion, both vertical and torsional motion).
  - Both vertical and torsional motion with the following wind speeds: 2.8 m/s, 4.1 m/s and 6.1 m/s.
- Both flaps are regulated, flap configuration 3: a_t = 6 and a_l =-6.
  - Free vibration (torsional motion, both vertical and torsional motion).
  - Both vertical and torsional motion with the following wind speeds: 2.5 m/s, 4.0 m/s, 5.9 m/s and 7.1 m/s.
- The flaps are not regulated, flap configuration 4: a_t =20 and a_l =-20.
  - Both vertical and torsional motion with the following wind speeds: 2.8 m/s, 4.2 m/s and 6.1 m/s.

4.4 Examples of damping experiments

In this section the torsional motion is shown as a function of time for wind speed 6.1 m/s and flap configurations 0, 2 and 4.

Figure 26 shows the torsional motion when the flaps are not regulated. The measurements are very noisy. During the first period the amplitude of the torsional motion is reduced from 2.6° to 2.4°, i.e. 8%. Figure 27 shows that flap configuration 2

is very efficient to control the torsional motion of the model. Even though the flaps are started slowly during the first second the amplitude of the torsional motion is reduced from 2.7° to 1.1°, i.e. 62%. Figure 28 shows the actual positions for the trailing flap for the example in figure 27. Figure 29 shows that the angular motion is growing, i.e. there is flutter, when flap configuration 4 is used.

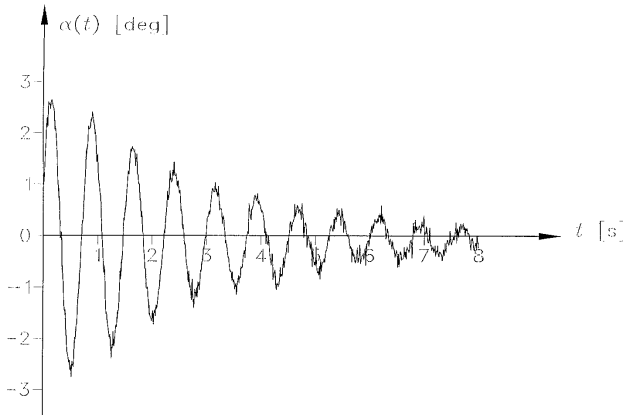

Figure 26. Example of torsional motion for flap configuration 0 and with wind speed 6.1 m/s.

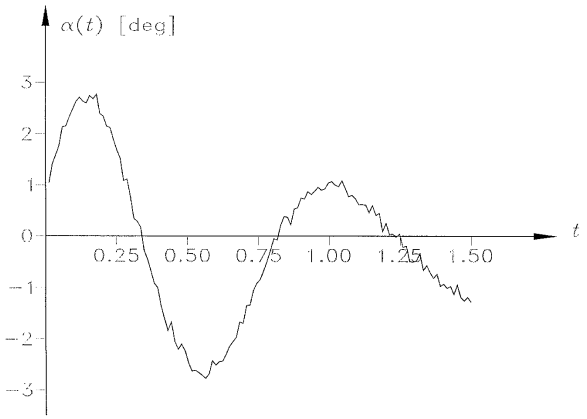

Figure 27. Example of torsional motion for flap configuration 2 and with wind speed 6.1 m/s.

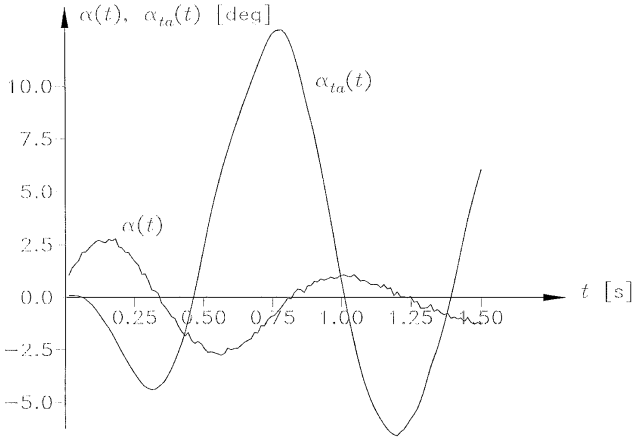

Figure 28. Example of torsional motion and actual flap positions for the trailing flap for flap configuration 2 and with wind speed 6.1 m/s.

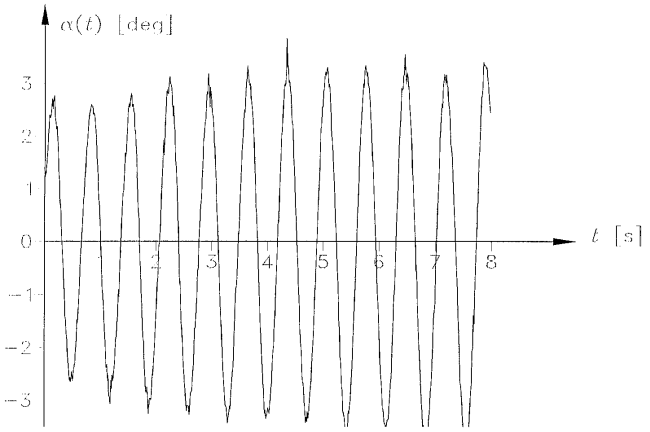

Figure 29. Example of torsional motion for flap configuration 4 and with wind speed 6.1 m/s.

4.5 Estimation of parameters

The following parameters are estimated based on the experiments:

- ω_z and ω_α: the circular frequencies for the vertical and torsional motion, respectively. The circular frequencies are estimated by counting a number of cycles for the time series $z(t)$ and $\alpha(t)$.
- ζ_α: the damping ratio for the torsional motion. The damping is estimated by using Hilbert transformation.
- a_{ta} and a_{la}: the actual amplitude amplification factors between the angular motion of the model and the actual positions of the flaps. These factors are estimated by optimization.
- φ_{ta} and φ_{la}: the phase angles between the angular motion of the model and the actual positions of the flaps. These factors are estimated by optimization.

The measured positions $z(t)$, $\alpha(t)$, $\alpha_{ta}(t)$ and $\alpha_{la}(t)$ are noisy, and therefore they are filtered. The filtered positions $z_f(t)$, $\alpha_f(t)$, $\alpha_{ta,f}(t)$ and $\alpha_{la,f}(t)$ are then used to estimate the above-mentioned parameters.

4.5.1 *Estimated Frequencies*

In figure 30 the circular frequencies for the vertical motion without wind are shown. The estimated frequencies are rather constant independently of the flap configuration and the main motion. The mean value of the circular frequency for the vertical motion is 5.2 rad/s.

The circular frequency for the vertical motion can be estimated without wind. When the wind is blowing the vertical motion becomes rather irregular until it is possible to estimate it again. The frequencies are shown in figure 31. With increasing wind velocity the circular frequency for the vertical motion is reduced. It is not possible to estimate the circular frequency for the vertical motion when flap configuration 2 is used.

In figure 32 the circular frequencies for the torsional motion without wind are shown. As for the vertical motion, the estimated frequencies are rather constant

independently of the flap configuration and the main motion. But there is a small tendency towards larger deviation of the results the more the flaps are moved. Note that flap configurations 1 and 3 specify small movement of the flaps. The mean value of the circular frequency for the torsional motion is 10.1 rad/s.

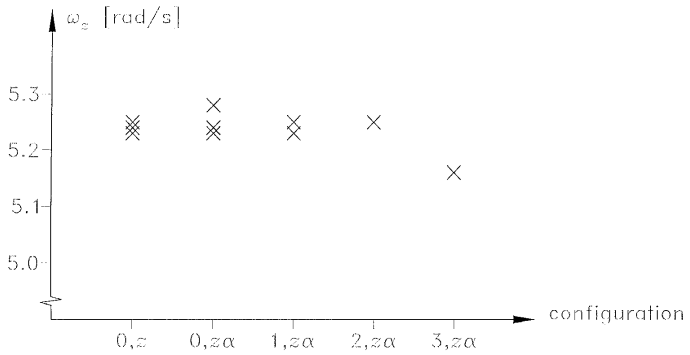

Figure 30. Estimated circular frequency for vertical motion without wind. The configuration is described by the flap configuration and the main motion, i.e. $z\alpha$ denotes a combined motion.

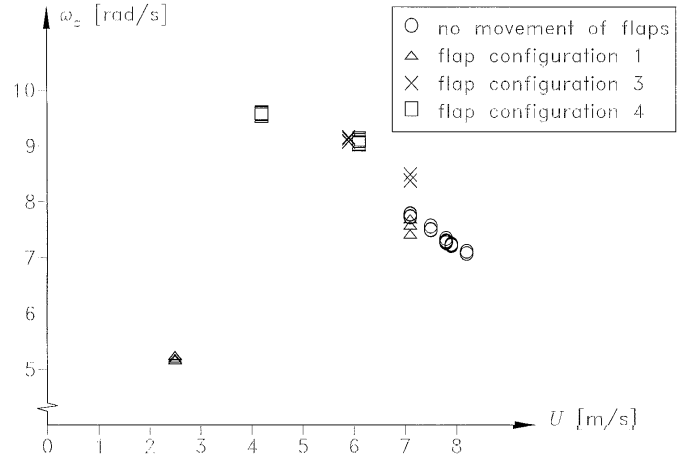

Figure 31. Estimated circular frequency for vertical motion with wind.

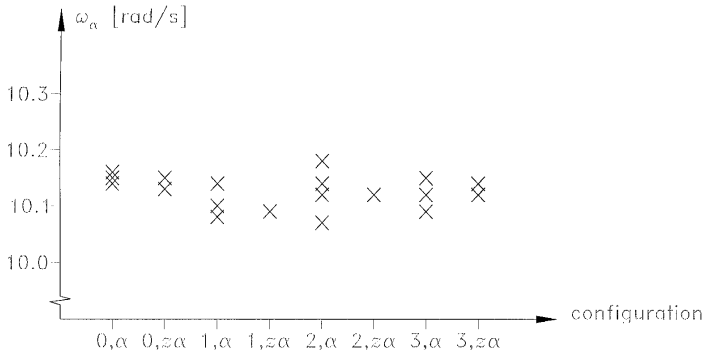

Figure 32. Estimated circular frequency for torsional motion without wind. The configuration is described by the flap configuration and the main motion, i.e. $z\alpha$ denotes a combined motion.

The circular frequencies for the torsional motion used to estimate the damping of the motion are shown in figure 33. Again, with increasing wind velocity the circular frequency for the torsional motion is reduced dependent on the flap configuration used.

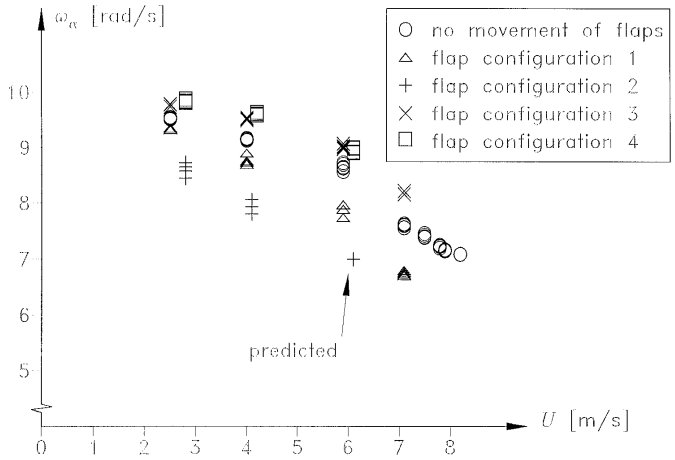

Fig. 33. Estimated circular frequency for torsional motion with wind. For the wind speed 6.1 m/s the motion is damped very fast when flap configuration 2 is used. The frequency for this wind speed and flap configuration is therefore predicted based on the estimated values for other wind speeds and flap configurations.

4.5.2 *Estimated Damping Ratios*

In figure 34 the damping ratios for the torsional motion without wind are shown. The estimated damping ratios are rather constant independently of the flap configuration and the main motion. But when the flaps are moved the damping ratio is larger for the main torsional motion than for the combined motion. Further, the more the flaps are turned the larger the damping ratio. The mean value of the damping ratio for the torsional motion is 0.008.

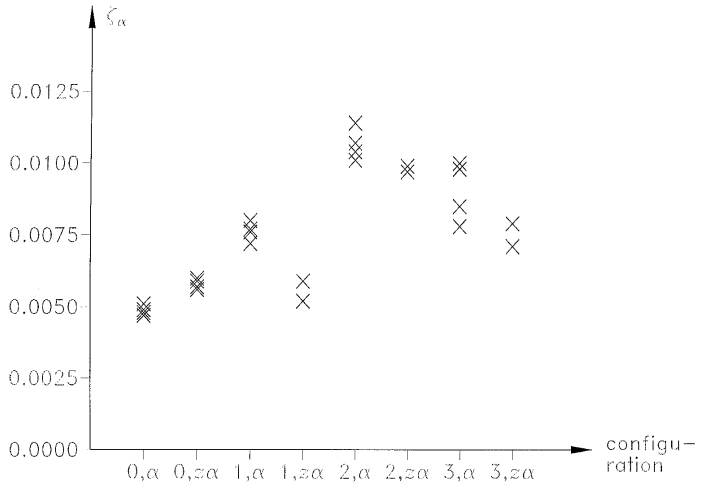

Figure 34. Estimated damping ratio for torsional motion without wind. The configuration is described by the flap configuration and the main motion, i.e. $z\alpha$ denotes a combined motion.

The damping ratio for the torsional motion for different flap configurations is shown as a function of the wind speed in figure 35. When flap configurations 1 and especially 2 are used the damping ratio is increased considerably, and when flap configurations 3 and 4 are used the damping ratio is decreased.

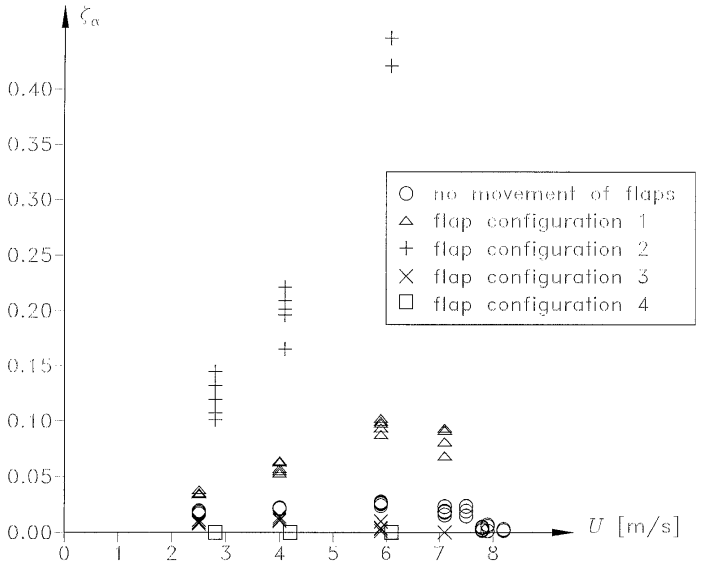

Figure 35. Estimated damping ratio for torsional motion with wind.

4.5.3 *Estimated Amplifications and Phases*
The torsional motion can be described by

$$\alpha(t) = A_\alpha(t)\cos(\omega'_\alpha t) \tag{80}$$

where $A_\alpha(t)$ is the amplitude of the envelope curve for the torsional motion and $\omega'_\alpha(t)$ is the circular eigenfrequency for the damped torsional motion.

The actual flap position for e.g. the trailing flap can be described by

$$\alpha_{ta}(t) = a_{ta}A_\alpha(t)\cos(\omega'_\alpha t - \varphi_{ta}) \tag{81}$$

where a_{ta} is the amplification factor and φ_{ta} is the phase angle for the trailing flap. The phase angle is equal to the damped circular frequency multiplied by the delay of the flap compared to the torsional motion, i.e. $\varphi_{ta} = \omega'_\alpha \Delta t_t$. In the same way the actual flap position for the leading flap can be described by the amplification factor a_{la} and the phase angle φ_{la}.

$$\alpha_{la}(t) = a_{la}A_\alpha(t)\cos(\omega'_\alpha t - \varphi_{la}) \tag{82}$$

where π. The amplifications a_{ta} and a_{la} and the phase angles φ_{ta} and φ_{la} are estimated for each flap configuration. The mean values are shown in table III.

Flap configuration	Amplification		Phase angles	
	a_{ta}	a_{la}	φ_{ta} [rad]	φ_{la} [rad]
0	0	0	—	—
1	1.9	2.0	4.5	4.5
2	3.4	3.6	4.6	4.6
3	2.0	2.0	1.5	1.5
4	*3.4* *	*3.6* *	*1.5* *	*1.5* *

Table III. Estimated amplification factors and phase angles. * For flap configuration 4 the parameters are predicted based on the results for other flap configurations.

As seen in table III, the trailing and leading flaps are moving with the same delay compared to the torsional motion. Note that the phase angles are equal because the angles of both flaps are positive downwards. Further, the amplitudes of the leading flap are slightly bigger than the amplitudes of the trailing flap. As expected the flap amplication factors are almost the same for flap configurations 1 and 3 and the phase angles are almost the same for flap configurations 1 and 2. Finally, as expected the difference between the phase angles for flap configurations 1 and 3 is approximately equal to π.

5. EXPERIMENTAL RESULTS COMPARED WITH THEORY

In this chapter the estimated parameters from the wind tunnel experiments are compared with the theoretical parameters by using the flat plate approximation described in chapter 2.

The flap configurations used in the wind tunnel experiments are shown in section 5.1. The wind dependent change of frequency and damping are compared with the theoretical values in sections 5.2 and 5.3. The optimal phase angles found in chapter 2 are in section 5.4 compared to the phase angles used during the experiments.

5.1 Flap configurations

The positive directions of the vertical and torsional motions of the bridge section model and of flap positions are shown in figure 36. The positive directions are equal to the positive directions defined in section 2. In chapter 4.3 the angle of the leading flap is defined as positive downwards, e.g. opposite to the definition used in this chapter.

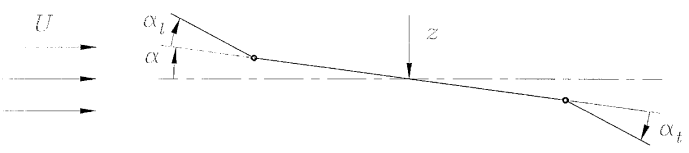

Figure 36. Definition of positive directions.

The positions of the flaps (with positive directions as shown in figure 36) at selected time instants for flap configurations 1-4 are shown in figures 37-40. When flap configuration 0 is used the flaps are not moved. Based on the torsional motion a(t), the actual flap positions at and al are calculated by using equations (81) and (82) with the

estimated parameters shown in table III for each of the flap configurations. At eight time steps during a period the angle of the model and flaps are shown in the upper part of figures 37-40.

For all flap configurations the flaps are near their horizontal positions when the angle of the torsional motion is maximum. Further, for all flap configurations the flaps are moved either up or down at the same time and the maximum angles of the flaps are when the model is approximately horizontal.

5.2 Wind dependent change of frequency

In figure 31 the circular frequency for the vertical motion as a function of the wind velocity is shown based on the wind tunnel experiments. The stiffness of the bridge section model with flaps for a pure vertical motion is

$$k_{z,U} = m\omega_z^2 - \frac{1}{2}\rho U^2 K_{z,U}^2 H_4^\star(K_{z,U}) \tag{83}$$

where

$$K_{z,U} = \frac{B\omega_{z,U}}{U} \tag{84}$$

where $\omega_{z,U}$ is the circular frequency of the vertical motion dependent on the wind velocity *U*. The wind dependent circular frequency of the vertical motion is

$$\omega_{z,U} = \omega_z \sqrt{1 - \frac{\rho B^2}{2m}\left(\frac{\omega_{z,U}}{\omega_z}\right)^2 H_4^\star\left(\frac{B\omega_{z,U}}{U}\right)} \tag{85}$$

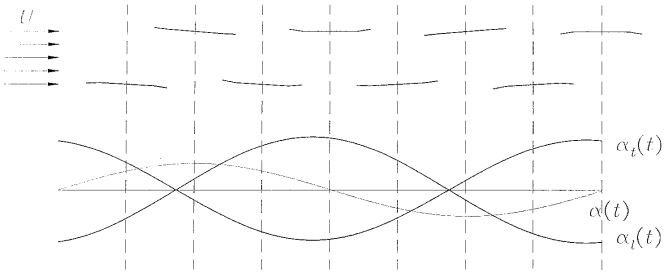

Figure 37. Movement of flaps for flap configuration 1.

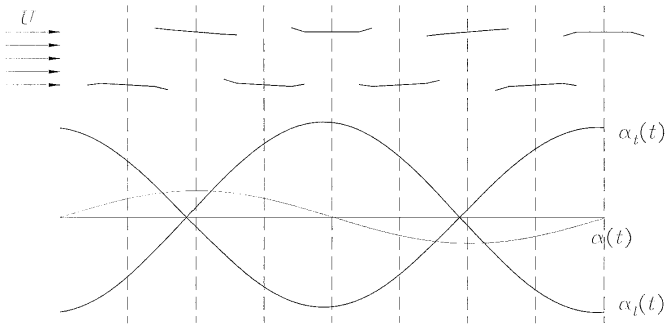

Figure 38. Movement of flaps for flap configuration 2.

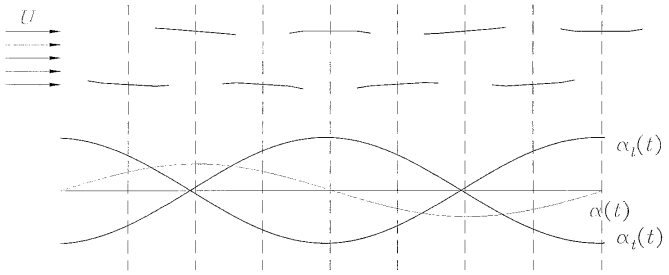

Figure 39. Movement of flaps for flap configuration 3.

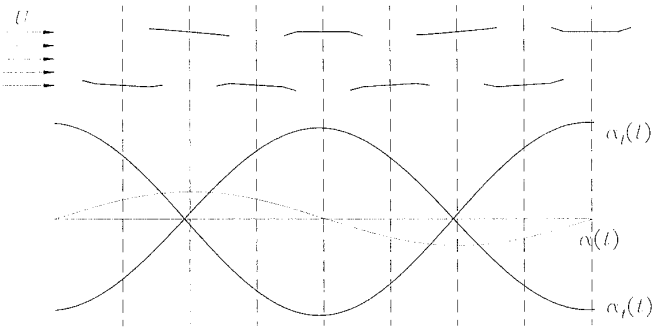

Figure 40. Movement of flaps for flap configuration 4.

According to Dyrbye & Hansen [10], the following approximation is quite accurate

$$\left(\frac{\omega_{z,U}}{\omega_z}\right)^2 H_4^\star\left(\frac{B\omega_{z,U}}{U}\right) \simeq H_4^\star\left(\frac{B\omega_z}{U}\right) \tag{86}$$

where ω_z is the circular eigenfrequency for the vertical motion, i.e. without wind. Equation (85) can thereby be written

$$\omega_{z,U} \simeq \omega_z \sqrt{1 - \frac{\rho B^2}{2m} H_4^\star\left(\frac{B\omega_z}{U}\right)} \tag{87}$$

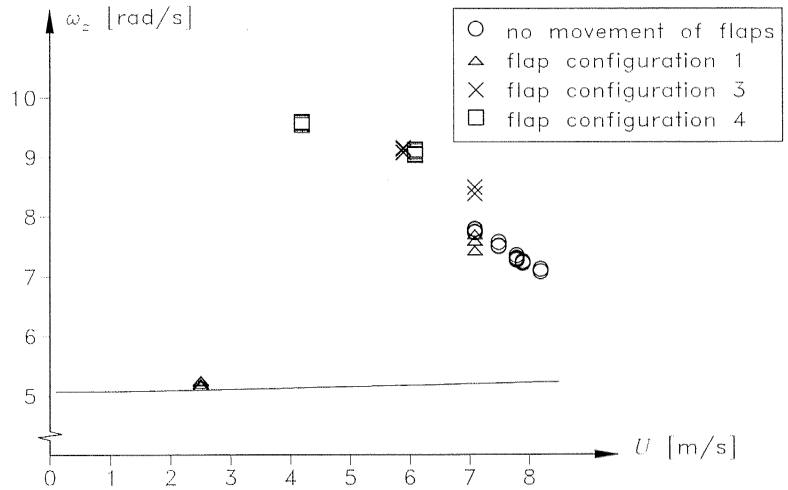

Figure 41. Theoretical and experimental circular frequency for vertical motion with wind.

Note, that the vertical frequency is independent of the flap configuration. The frequencies estimated based on the experimental data are compared to the theoretical frequencies by using Theodorsen's theory for a flat plate, see figure 41.

As seen in figure 41, only the first values of the circular frequency for the vertical motion for flap configuration 1 are on the theoretical curve. However, the theoretical curve for pure vertical motion does not agree with the binary flutter theory either, since the flutter wind velocity for the bridge section model is ω_f = 6.62 rad/s and the flutter wind velocity is U_f = 8.18 m/s, see section 2.2. This may be explained by the pure vertical motion assumption for equation (87) contrary to the combined vertical and torsional motion for binary flutter. Perhaps the results would fit better if a Fourier analysis had been made. Also, for the experimental data the vertical frequency is independent of the flap configuration.

In figure 33 the circular frequency for the torsional motion as a function of the wind velocity is shown based on the wind tunnel experiments. The stiffness of the bridge section model with flaps for a pure torsional motion is

$$k_{\alpha,U} = I\omega_\alpha^2 - \frac{1}{2}\rho U^2 K_{\alpha,U}^2 B^2 A_3^{\star'}(K_{\alpha,U}) \tag{88}$$

where

$$K_{\alpha,U} = \frac{B\omega_{\alpha,U}}{U} \tag{89}$$

where $\omega_{\alpha,U}$ is the circular frequency of the torsional motion dependent on the wind velocity U
and

$$\begin{aligned} A_3^{\star'}(K) = {} & A_3^\star(K) - A_5^\star(K)a_t\sin(-\varphi_t) + A_6^\star(K)a_t\cos(-\varphi_t) - \\ & A_7^\star(K)a_l\sin(-\varphi_l) + A_8^\star(K)a_l\cos(-\varphi_l) \end{aligned} \tag{90}$$

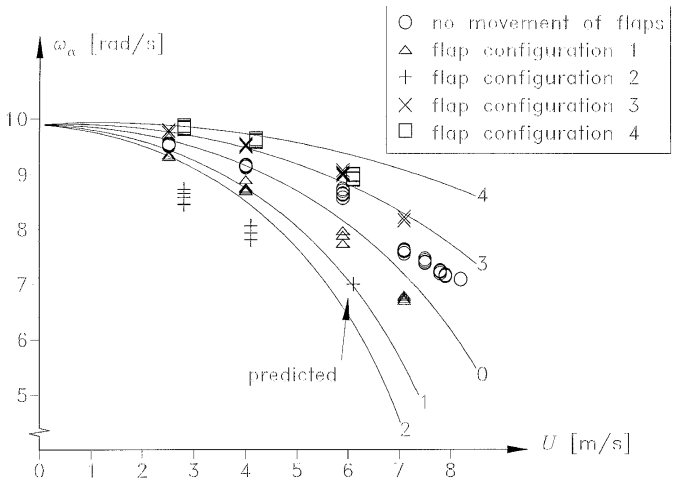

Figure 42. Theoretical and experimental circular frequency for torsional motion with wind for flap configuration 0-4. The number at the end of a solid line denotes the actual flap configuration.

The wind dependent circular frequency of the torsional motion is

$$\omega_{\alpha,U} = \omega_\alpha \sqrt{1 - \frac{\rho B^4}{2I}\left(\frac{\omega_{\alpha,U}}{\omega_\alpha}\right)^2 A_3^{\star\prime}\left(\frac{B\omega_{\alpha,U}}{U}\right)}$$
$$\simeq \omega_\alpha \sqrt{1 - \frac{\rho B^4}{2I} A_3^{\star\prime}\left(\frac{B\omega_\alpha}{U}\right)} \qquad (91)$$

where ω_α is the circular eigenfrequency for the torsional motion, i.e. without wind. Note that the torsional frequency is dependent on the flap configuration specified by the flap amplification factors a_t and a_l and the phase angles φ_t and φ_l. The frequencies estimated based on the experimental data are compared to the theoretical frequencies by using the aerodynamic derivatives for a flat plate for flap configurations 0-4, see figure 42.

As seen in figure 42 the estimated values generally follow the theoretical curves for wind velocities below approximately 5 m/s. The only exception is flap configuration 2, but the deviations for this flap configuration can be caused by the relatively short time series because of the effective damping. The pure torsional motion does not completely agree with the binary flutter theory but the fit is much better than for the pure vertical motion described above.

5.3 Wind dependent change of damping

In figure 35 the damping ratio for the torsional motion is shown as a function of the wind velocity based on the wind tunnel experiments. The damping ratio can also be estimated by the AMC method described in section 2.3. The damping ratio $g(U)$ defined in section 2.3 as twice the necessary structural damping is replaced by $-0.5g(U)+\zeta_{\alpha,0}$ to be compared with the experimental damping ratios. The mean value of the damping ratio without wind is $\zeta_{\alpha,0} = 0.008$, see section 4.5.2.

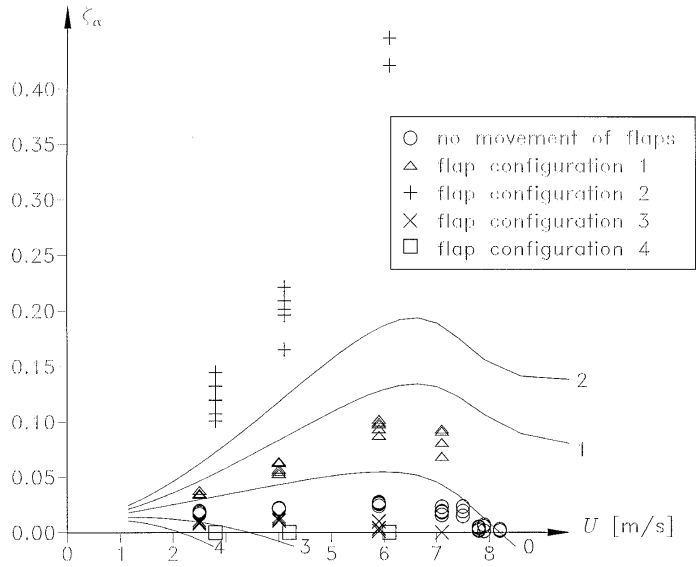

Fig. 43. Theoretical and experimental damping for torsional motion with wind for flap configuration 0-4. The number at the end of a solid line denotes the actual flap configuration.

The damping ratios estimated based on the experimental data are compared to the

theoretical damping ratios by using the AMC method and the aerodynamic derivatives for a flat plate for flap configurations 0-4, see figure 43.

As seen in figure 43, the experimental damping ratio is smaller for flap configuration 0 and 1 than the theoretical damping ratio but the shape of the curve is almost the same. For flap configuration 2 the experimental damping ratio exceeds the theoretical ratio. For flap configurations 1 and 2 the theoretical curves show that no binary flutter will occur. For the flap configurations 3 and 4 the flutter wind velocity is decreased compared to flap configuration 0, where the flaps are not moved.

5.4 Optimal flap positions

There is no guarantee that the phase angles used in the wind tunnel experiments $\varphi_l \cong 1.5$ rad and $\varphi_t \cong 4.5$ rad are optimal. When the flat plate approximation is used then the optimal phase angles are about $\varphi_l \cong 3\pi/6 = 1.57$ rad and $\varphi_t \cong 8\pi/6 = 4.19$ rad for small values of flap amplification factors al and at, see section 2.2. Based on the performed experiments it is not possible to conclude which phase angles are optimal for the model, and therefore, it is also not possible to predict the optimal effect of the flap control system.

6. CONCLUSION

The main conclusions are summarized as:

- Both theoretically and experimentally the flap control system was very efficient to limit the vibrations of the bridge section model.
- Theoretically, long flaps are more efficient than short flaps.
- Theoretically, the trailing flap is more efficient than the leading flap. It is optimal to use both flaps.
- It is very important that the flaps are regulated as specified by the selected control algorithm as the flutter wind velocity can be decreased if the flap configuration is unfavourable.

ACKNOWLEDGEMENT

The work has been sponsored by the Danish Technical Research Council within the programme Structural Safety and Reliability.

REFERENCES

[1] H.I. Hansen, 1998. Active Vibration Control of Long Suspension Bridges.. Ph.D. thesis, Aalborg University, Denmark.

[2] W. Brown, 1996. Development of the Deck for the 3300 m Span Messina Crossing. In Proceedings of the 15th Congress of IABSE, pages 1019-1030.

[3] N. Gimsing, 1992. Large Bridges of the Future. In Aerodynamics of Large Bridges, pages 295-304.

[4] M. Astiz, 1996. Wind Related Behaviour of Alternative Suspension Systems. In Proceedings of the 15th Congress of IABSE, pages 1079-1090.

[5] K. Ostenfeld, 1996. Comparison between Different Structural Solutions. The Great Belt Project. In Proceedings of the 15th Congress of IABSE, pages 1063-1078.
[6] K. Ostenfeld and A. Larsen, 1992. Bridge Engineering and Aerodynamics. In Aerodynamics of Large Bridges, pages 3-22.
[7] H. Madsen and P. Ostenfeld-Rosenthal, 1992. Wind Criteria for Long Span Bridges. In Aerodynamics of Large Bridges, pages 33-43.
[8] European Patent Specification, 1996. A System and a Method of Counteracting Wind induced Oscillations in a Bridge Girder. EP 0 627 031 B1. Bulletin 1996/24.
[9] R. Scanlan, 1992. Wind Dynamics of Long-Span Bridges. In Aerodynamics of Large Bridges, pages 47-57. [16] E. Dowell, H. Curtiss, R. Scanlan, and F. Sisto, 1978. A Modern Course in Aeroelasticity. Sijthoff & Noordhoff.
[10] C. Dyrbye and S. Hansen, 1996. Wind Load on Structures. John Wiley & Sons.
[11] E. Simiu and R. Scanlan, 1986. Wind Effects of Structures. John Wiley & Sons, second edition.
[12] A. Larsen and J. Walther, 1996. A New Computational Method for Assessment of the Aeroelastic Stability of Long Span Bridges. In Proceedings of the 15th Congress of IABSE, pages 93-98.
[13] T. Theodorsen, 1935. General Theory of Aerodynamic Instability and the Mechanism of Flutter, pages 22-31. AIAA Selected Reprint Series, Vol. V, Aerodynamic Flutter. American Institute of Aeronautics and Astronautics, 1976. NACA Rep. No. 496 (1935).
[14] E. Dowell, H. Cortiss, R. Scanlan & F. Sisto, 1978. A Modern Course in Aeroelasticity, Sijthoff & Noordhoff.
[15] Y. Fung, 1955. An Introduction to the Theory of Aeroelasticity. John Wiley & Sons.
[16] T. Soong, 1990. Active Structural Control. Theory and Practice. Longman Scientific and Technical.
[17] H.I. Hansen, P. Thoft-Christensen, P.A. Mendes and F.A. Branco, 2000. Wind-Tunnel Tests of a Bridge Model with Active Vibration Control. Structural Engineering International, Volume 10, Number 4, pages 249-253.
[18] Z. Wu, T. Soong, V. Gattulli, and R. Lin, 1995. Nonlinear Control Algorithms for Peak Response Reduction. State University of New York at Buffalo, Department of Civil Engineering, Buffalo, New York. Technical Report NCEER-95-0004.